Received: 1 June 2023 | Revised: 28 September 2023 | Accepted: 18 November 2023

DOI: 10.1111/ffe.14210

ORIGINAL ARTICLE

FFEMS Fatigue & Fracture of Engineering Materials & Structures WILEY

Predicting microstructurally sensitive fatigue-crack path in WE43 magnesium using high-fidelity numerical modeling and three-dimensional experimental characterization

Brian R. Phung[1] | **Duncan A. Greeley**[2] | **Mohammadreza Yaghoobi**[2] | **Jacob F. Adams**[2] | **John E. Allison**[2] | **Ashley D. Spear**[1]

[1]Department of Mechanical Engineering, University of Utah, Salt Lake City, Utah, USA

[2]Department of Materials Science and Engineering, University of Michigan, Ann Arbor, Michigan, USA

Correspondence
Brian R. Phung, Department of Mechanical Engineering, University of Utah, 1495 E 100 S, Salt Lake City, UT 84112, USA.
Email: brian.phung@utah.edu

Funding information
National Science Foundation, Grant/Award Numbers: CMMI-1629660, CMMI-1752400

Abstract

Microstructurally small fatigue-crack growth in polycrystalline materials is highly three-dimensional due to sensitivity to local microstructural features (e.g., grains). One requirement for modeling microstructurally sensitive crack propagation is establishing the criteria that govern crack evolution, including crack deflection. Here, a high-fidelity finite-element modeling framework is used to assess the performance and validity of various crack-growth criteria, including slip-based metrics (e.g., fatigue-indicator parameters), as potential criteria for predicting three-dimensional crack paths in polycrystalline materials. The modeling framework represents cracks as geometrically explicit discontinuities and involves voxel-based remeshing, mesh-gradation control, and a crystal-plasticity constitutive model. The predictions are compared to experimental measurements of WE43 magnesium samples subject to fatigue loading, for which three-dimensional grain structures and fatigue-crack surfaces were measured post-mortem using near-field high-energy x-ray diffraction microscopy and x-ray computed tomography. Findings from this work are expected to improve the predictive capabilities of simulations involving microstructurally small fatigue-crack growth in polycrystalline materials.

KEYWORDS

crack propagation and arrest, crystal plasticity, finite elements, grain boundaries, microstructures

1 | INTRODUCTION

Microstructurally small (short) crack growth, defined as crack propagation while the crack size is on the order of the size of local microstructural features,[1] can account for a significant portion of a component's total fatigue life.[2] Fatigue-crack growth approximations that assume that cracks grow in a self-similar manner and that the size of the plastic zone ahead of the crack front is small relative to the crack size (e.g., Paris' Law[3]) are unable to capture crack propagation behavior at this length scale. Rather, short cracks are well known to be heavily influenced by the local microstructure features, such as crystallographic slip in grains,[4] grain boundaries,[5] and relative grain misorientation.[6,7] In experiments, the observed complexity of short-crack surfaces in three

dimensions is commonly attributed to effects of the local microstructure.[8–11] Due to their complexity, understanding and predicting the behavior of short cracks remains an open area of study.

Developments in crystal plasticity models and computational resources have popularized the use of numerical modeling to investigate short-crack behavior. It is commonly reported that field variables (e.g., stress and strain) ahead of a crack front are affected by the local microstructure[12–14] and can be correlated to short-crack nucleation or propagation behavior. Using crystal plasticity and the extended finite element method, Zhang and Dunne[14] found variations in the stress field ahead of the crack front when the crack front impinges on a grain boundary with mismatching twist. Hochhalter et al[15] found a correlation between the local maximum tangential stress in Aluminum 7075-T651 and the crack nucleation direction. However, stress and strain do not explicitly convey the slip activity that influences short-crack behavior. For this, slip-based damage parameters, or fatigue-indicator parameters (FIPs), have been developed and commonly used as a measure of driving force for short-crack nucleation and propagation.[16,17] Hochhalter et al[15,18] studied the relationship between a set of FIPs and short-crack nucleation behavior in Aluminum 7075-T651 and found that most FIPs perform similarly.[18] Castelluccio and McDowell[4] correlated values of the Fatemi-Socie FIP[19] to crack-tip displacement, and thus the crack-growth rate; further works based on the Fatemi-Socie FIP have been used to assess short-crack-growth rate.[20,21]

While the examples described above illustrate efforts to predict the nucleation or growth rate of short cracks using numerical simulation, studies involving the growth direction of short cracks (i.e., crack path) are more limited. In two dimensions, Srivastava et al[22] used a graph-based approach to predict crack path in an underaged magnesium WE43 thin-foil sample. Refs.,[23,24] used a Fatemi-Socie-based[19] FIP to predict crack-growth rate and direction in body-centered cubic single crystals. In three dimensions, data-driven methods have been employed by Pierson et al[25] to study the correlation between micromechanical fields in an uncracked experimentally characterized aluminum polycrystal and observed crack path, and found spatial gradients of the micromechanical fields yielded a higher correlation than the fields themselves. In later work, Pierson et al[26] proposed a machine-learning-based method to predict crack path in the same dataset but suggested that more experimental data would be needed to improve predictions. Using crystal plasticity fast-Fourier transform simulations and a probabilistic Bayesian model, Rovinelli et al[27] found FIPs correlated with an experimentally observed short-crack path in a beta-titanium alloy. Proudhon et al[28] simulated short-crack growth in the aforementioned beta-titanium alloy; while they cited similarities between the simulated crack surface and generally observed short-crack growth behavior, they did not explicitly benchmark the Fatemi-Socie-based[19] FIP against an experimentally observed crack surface as performed in Rovinelli et al.[27]

The critical assessment of potential crack-deflection criteria for short cracks requires both experimental observations of crack growth in three-dimensional microstructures and a numerical toolset capable of quantifying micromechanical fields ahead of microstructurally short cracks. For the former requirement, experimental techniques such as near-field high-energy x-ray diffraction microscopy (nf-HEDM)[29] and x-ray computed tomography (CT) enable the characterization of three-dimensional microstructures containing observed crack surfaces, thereby allowing for predictions from candidate crack-deflection criteria to be compared to experimentally observed crack paths. Regarding the latter, micromechanical fields are important as they play a role in governing crack path. For instance, Greeley et al[30] recently performed a statistical analysis of observed three-dimensional crack paths in experimentally measured magnesium WE43 samples by considering 24 purely crystallographic and geometric features (e.g., orientation of slip planes in grains just ahead of the crack, angle between crack plane and grain boundaries just ahead of the crack, misorientation between neighboring grains just ahead the crack, etc.). They found that geometric compatibility parameters had lower correlation with observed crack path than did the average Schmid factor in grains just ahead of the crack front, which they attributed in large part to heterogeneity in the local stress state, something that was not captured in their analysis. To account for micromechanical fields ahead of the crack front, the authors previously developed a voxel-based remeshing framework[31] to represent and propagate complex three-dimensional cracks through heterogeneous (viz., polycrystalline) materials. The authors later implemented a mesh-gradation tool focused specifically on microstructures with defects (e.g., cracks)[32] to reduce the computational expense associated with crystal-plasticity constitutive modeling and high-resolution finite-element (FE) meshes. These tools and modern high-performance computing make the investigation of crack-deflection criteria in three-dimensional polycrystals computationally tractable.

The objective of this work is two-fold: (1) to demonstrate the capability of the recently implemented high-fidelity, crack-simulation framework[31,32] applied to experimentally measured microstructures of underaged magnesium WE43[8,30] and (2) to assess the performance of several potential crack-deflection criteria for predicting three-dimensional fatigue-crack path in the experimentally measured microstructures.

2 | METHODS

Four experimental datasets are used to demonstrate the modeling capabilities of a high-fidelity crack-simulation framework and to investigate potential crack-deflection (i.e., kink angle) criteria based on the numerical simulations. Grain structure and crack surfaces from three underaged magnesium WE43 thin-foil samples are reproduced directly in numerical simulations to preliminarily assess candidate criteria and establish proposed modifications to the criteria. The predictive capabilities of the modified criteria are then tested by performing blind predictions of three-dimensional crack growth in an experimentally characterized underaged magnesium WE43 polycrystal extracted from a cylindrical fatigue sample. Section 2.1 provides a brief description of the experimental datasets, and Sections 2.2–2.4 detail the numerical simulations.

2.1 | Overview of experimental data and reconstruction methods

2.1.1 | Magnesium WE43 thin-foil samples

In previous work by Adams,[8] three magnesium alloy WE43 thin-foil samples were subjected to ultrasonic fatigue loading to investigate short-crack growth. The samples were machined into dog-bone-shaped specimens using electrical discharge machining and polished to approximately 150 μm thickness. Notches were placed perpendicular to the loading direction, and the samples were cyclically loaded to failure with a maximum nominal stress of 60 MPa and a load ratio $R = 0.1$. Full details of these experiments can be found in Adams.[8] The samples were later characterized post-mortem using nf-HEDM and x-ray CT at the 1-ID beamline at the Advanced Photon Source, Argonne National Laboratory, to obtain each foil sample's grain structure and fracture surfaces.

Following the methods reported in literature,[11,33] reconstructed data from the post-mortem nf-HEDM and x-ray CT measurements were merged to produce a fully populated, voxel-based volume representing the uncracked grain structure for a sub-region containing the crack-initiation site of each foil sample. Following the work by Greeley et al,[30] grains immediately adjacent to opposing sides of the fracture surface were merged into a single grain if their crystallographic misorientation was less than or equal to 15°. The resulting voxelized volumes and their associated fracture surfaces are shown in Figure 1.

2.1.2 | Magnesium WE43 cylindrical sample

Also, in previous work by Adams,[8] three-dimensional short-crack growth in an underaged magnesium alloy WE43 cylindrical sample was experimentally characterized. The material was machined into a cylindrical

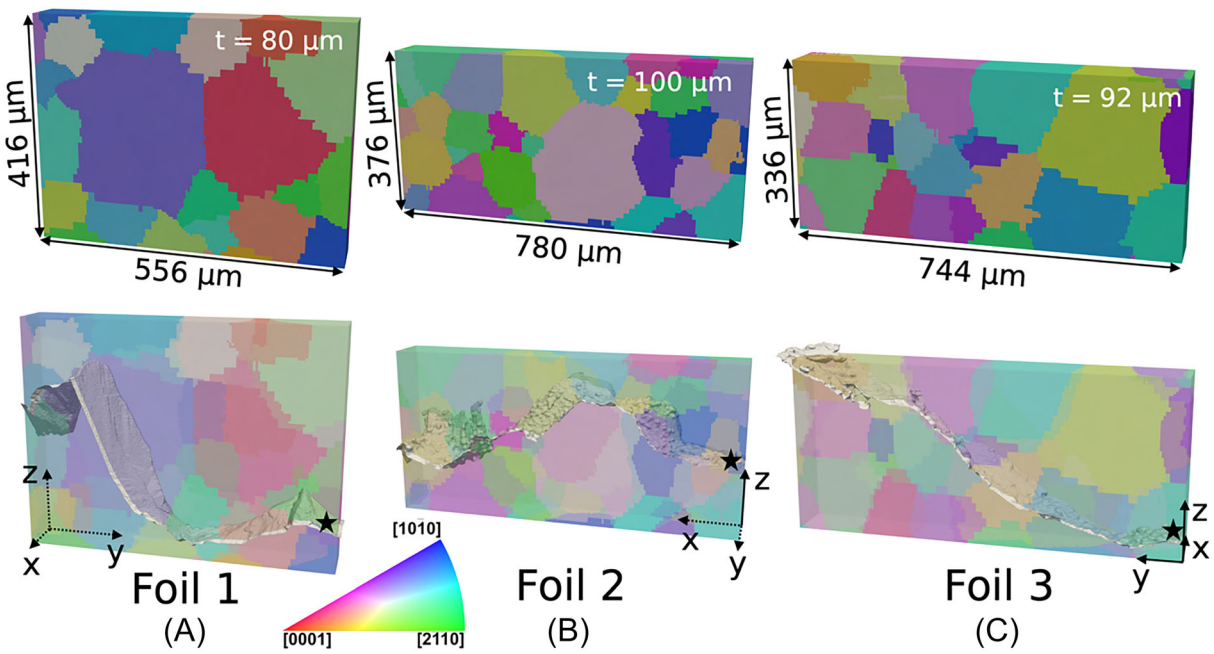

FIGURE 1 Voxel-based microstructures of underaged magnesium WE43 thin-foil samples from Adams[8] reconstructed from near-field HEDM measurements, with accompanying crack surfaces from x-ray CT. Three foils are used in this study: (A) Foil 1, (B) Foil 2, and (C) Foil 3. Star indicates crack initiation locations. The direction of x and y axes vary for each foil due to differences in reference frame during experimental characterization. [Colour figure can be viewed at wileyonlinelibrary.com]

specimen with a gauge section diameter of 4 mm and machined surface flats, as shown in Figure 2A. A micro-notch approximately 100 μm long, 6 μm wide, and 40 μm depth was machined into the gauge flat and was aligned with the basal plane of the grain containing the notch. The notched grain was selected due to a high nominal basal Schmid factor. The sample was cyclically loaded to failure with a maximum nominal stress of 85MPa with a load ratio $R = -1$. The grain structure and the fracture-surface morphology in the neighborhood of the machined micro-notch were obtained using nf-HEDM and x-ray CT, as detailed by Adams.[8] The high-resolution fracture surface and the aligned halves are shown in Figure 2B.

Following the methods reported in literature,[11,33] reconstructed data from the post-mortem nf-HEDM and x-ray CT measurements were merged to produce a fully populated, voxel-based volume representing the uncracked grain structure for a sub-region of the cylindrical sample containing the notch. Following the work by Adams,[8] a 30° misorientation threshold was applied to merge grains immediately adjacent to opposing sides of the fracture surface into a single grain. The final reconstructed volume is shown in Figure 2C, and the relative location of the fracture surface in the volume is shown in Figure 2D.

2.2 | General overview of crack-simulation framework and constitutive model

2.2.1 | Model generation and crack propagation

A previously developed voxel-based remeshing framework with mesh-gradation control[31,32] is used to assess

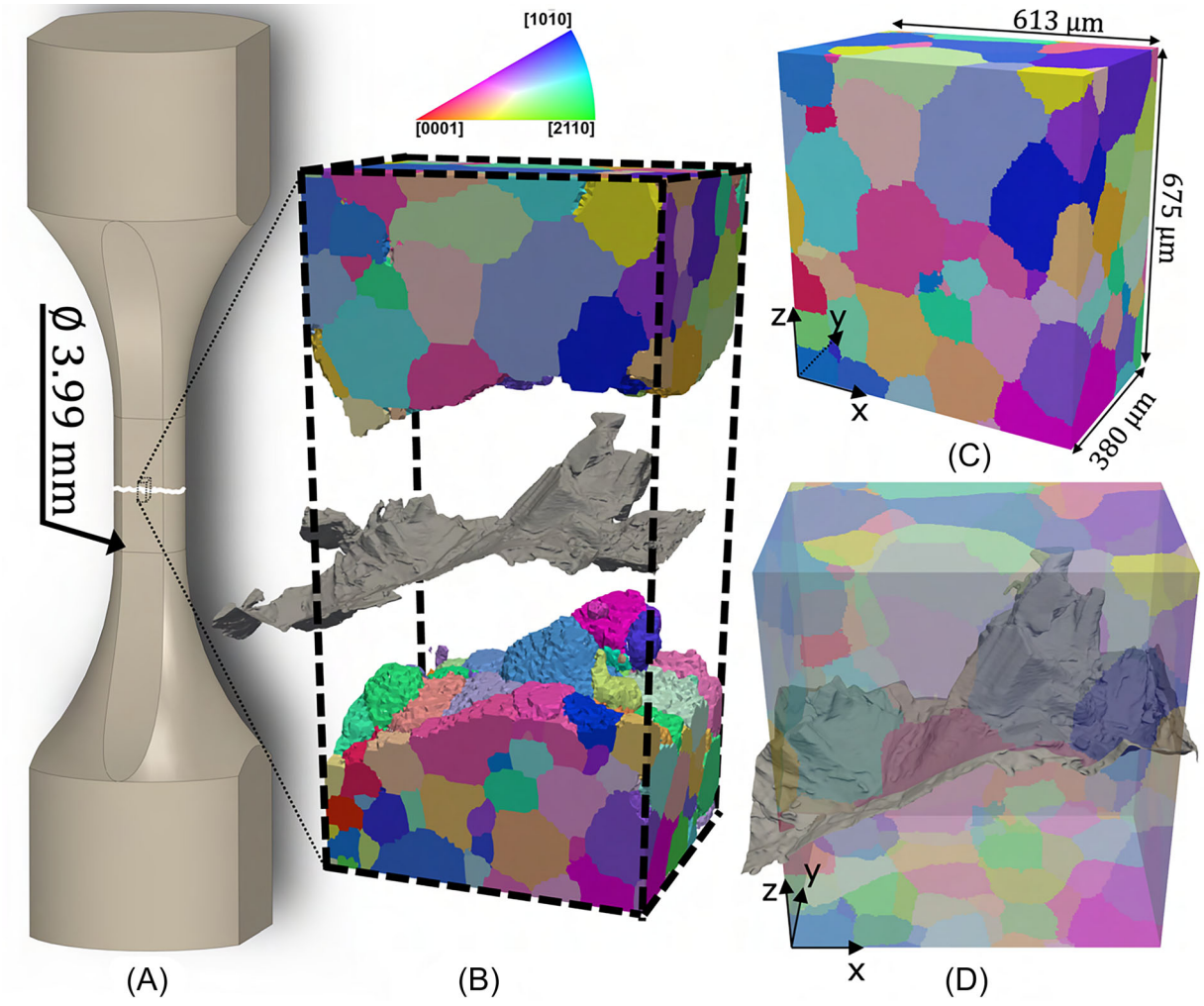

FIGURE 2 (A) Magnesium WE43 cylindrical fatigue sample from Adams.[8] (B) Two halves extracted from the fatigue-failed cylindrical fatigue sample imaged with near-field HEDM, with accompanying crack surface imaged with x-ray CT. (C) Voxel-based volume of approximated uncracked microstructure. (D) Overlay of experimentally measured crack surface for reference. [Colour figure can be viewed at wileyonlinelibrary.com]

the performance and validity of potential crack-deflection criteria in the underaged magnesium WE43 datasets. Before describing the specific application of the framework to the experimental datasets, a general overview of the framework is provided and summarized in Figure 3.

The microstructure, crack geometry, and crack evolution are tracked in a three-dimensional grid with associated attributes, that is, a voxel-based representation (VBR). Each voxel has an associated ID that encodes both the parent grain ID and the relative position of the voxel with respect to the crack surface at a given time in the history of the crack. For example, as illustrated in Figure 3B, voxel IDs *100245* and *200245* belong to parent grain ID *245* and are located below and above the crack surface, respectively. As cracks are predicted to evolve within the microstructure, the voxel IDs are updated accordingly.

The VBR is converted into a conformal FE mesh. First, the software DREAM.3D[34] is used to convert the VBR into a uniformly sized surface mesh that conforms, with optional smoothing, to both the grain boundaries and crack surface. The surface mesh is then converted into a volume mesh. The output surface mesh (and, consequently, the volume mesh) is tied to the resolution of the VBR, which must be relatively high to ensure the crack surface is represented with high fidelity. However, maintaining this level of resolution can render crack-propagation simulations intractable. To improve computational efficiency, a surface-mesh gradation tool[32] is invoked that refines surface elements around the crack front and coarsens surface elements in the far field. The resulting surface mesh from the mesh-gradation tool is converted into gradated volume meshes using Tetgen,[35] where the volume elements are refined near the crack front and coarsened in the far field. Finally, the nodes along the crack surface are duplicated to create a geometric discontinuity in the FE mesh, as shown in Figure 3C.

Once a FE mesh is generated, a simulation is run with the crack represented as a geometric discontinuity with traction-free surfaces in the microstructure, and new crack-front points are determined based on user-specified growth criteria. Field variables associated with these user-specified crack-growth criteria are retrieved from the FE results along a semi-circular probe path, Φ, about each crack-front point, shown in Figure 3D. The results are extracted using the path feature in ABAQUS,[36] which uses element shape functions to interpolate solution variables from neighboring integration points. Each semi-circular probe with radius, R_p, is formed in a plane parallel to the loading direction that contains the crack origin, O, and current crack-front point, as shown in Figure 3D. Upon evaluating the crack-growth criteria, a uniform filter is applied to kink-angle predictions. New crack-front points are calculated from the filtered-kink angles by extending each crack-front point by an increment, da, in the plane of the probe path in the direction of the predicted deflection angle, ϕ, as shown in Figure 3E. The new crack-front points are subsequently passed through a Savitzky-Golay filter.[37]

Once new crack-front points are determined, the crack surface is extended, and the VBR is updated accordingly, as shown in Figure 3B. Where the crack has extended, voxel IDs in the previously uncracked volume are updated with new identifiers to encode information about the new crack surface. From here, the process repeats to simulate new increments of crack growth. The reader is referred to previous studies[31,32] for additional details about the crack-simulation framework.

2.2.2 | Crystal plasticity constitutive model

A rate-dependent crystal-plasticity model based on Kalidindi et al,[38] originally implemented in the open-source software PRISMS-Plasticity,[39] was implemented as a User Material (UMAT) in the Abaqus FE solver.[36] The constitutive model represents slip-based deformation[†] and relies on a multiplicative decomposition of the deformation gradient tensor:

$$\boldsymbol{F} = \boldsymbol{F}^{\mathrm{e}}\boldsymbol{F}^{\mathrm{p}}, \tag{1}$$

where $\boldsymbol{F}^{\mathrm{e}}$ and $\boldsymbol{F}^{\mathrm{p}}$ are the elastic and plastic deformation gradient tensors, respectively. The plastic velocity gradient tensor in the isoclinic intermediate configuration can be defined as:

$$\boldsymbol{L}^{\mathrm{p}} = \dot{\boldsymbol{F}}^{\mathrm{p}}\boldsymbol{F}^{\mathrm{p}-1} = \sum_{\alpha=1}^{n_s} \dot{\gamma}^{\alpha}\boldsymbol{m}_{\boldsymbol{0}}^{\boldsymbol{\alpha}} \bigotimes \boldsymbol{n}_{\boldsymbol{0}}^{\boldsymbol{\alpha}}, \tag{2}$$

where $\dot{\gamma}^{\alpha}$ is the slip rate on slip system α and $\boldsymbol{n}_{\boldsymbol{0}}^{\boldsymbol{\alpha}}$ and $\boldsymbol{m}_{\boldsymbol{0}}^{\boldsymbol{\alpha}}$ are the slip plane normal and slip direction, respectively, of slip system α. A phenomenological flow rule governs the slip rate:

$$\dot{\gamma}^{\alpha} = \dot{\gamma}_0 \left(\frac{|\tau^{\alpha}|}{s^{\alpha}}\right)^{(1/m)} \mathrm{sign}(\tau^{\alpha}), \tag{3}$$

[†]Experimental measurements on which this work is based found no twin orientations in the far-field HEDM reconstructions and no wide lenticular low-confidence bands, indicating unindexed large twin lattices that constitute an appreciable volume of the parent grain were not detected in the near-field HEDM reconstructions.[30] However, very small twins with thicknesses on the order of the spatial resolution of the near-field reconstruction would likely not be able to be identified in the near-field data.

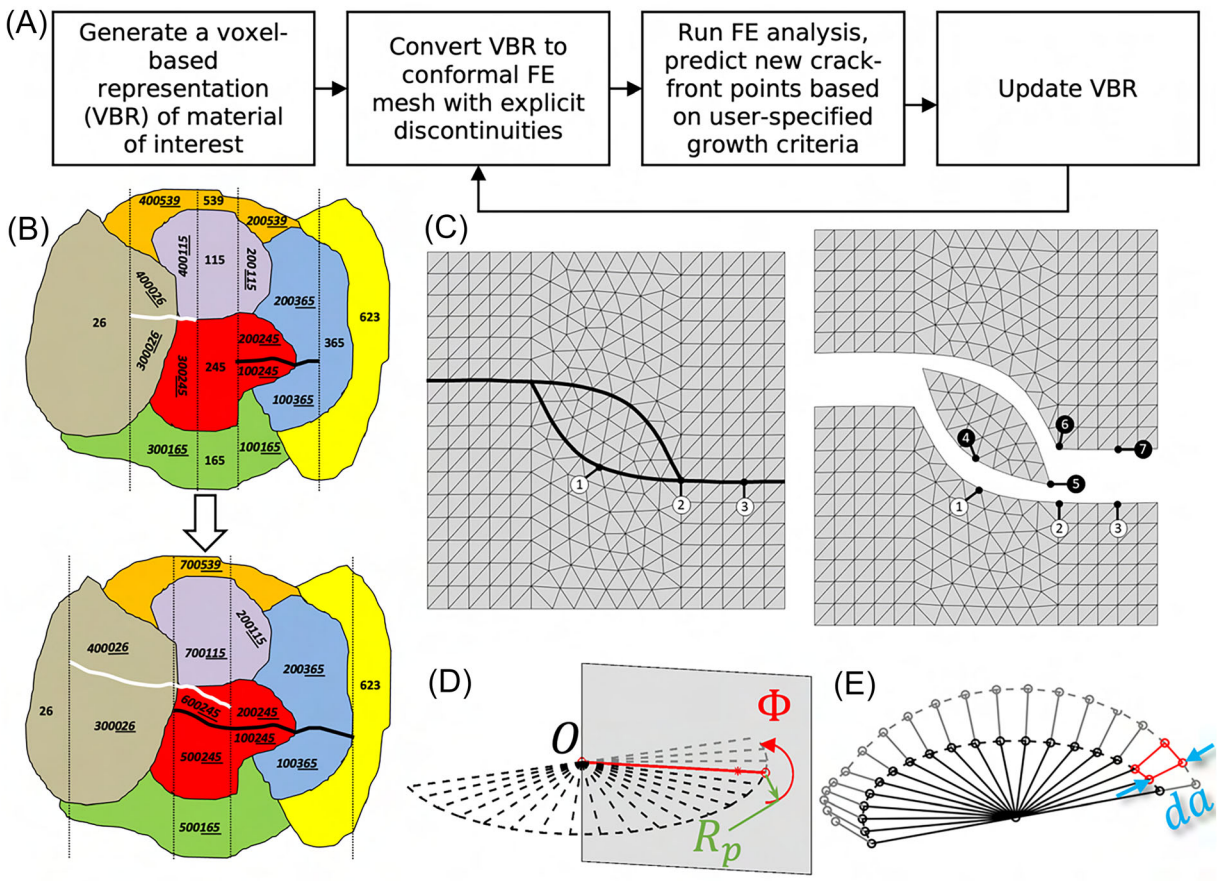

FIGURE 3 (A) Workflow overview of the voxel-based remeshing framework. (B) Voxels are labeled by grain ID, and the crack is represented with unique identifiers. (C) Cracks are represented in the mesh as geometric discontinuities via node duplication. (D) Representative field-variable probing strategy, where Φ is the probe path and R_p is the probe radius. (E) Example of crack extension in the framework, where crack front points are extended by increment da along the kink-angle direction. [Colour figure can be viewed at wileyonlinelibrary.com]

where $\dot{\gamma}_0$ is the reference slip rate and m is a strain-rate sensitivity parameter; τ^α and s^α are the resolved shear stress and slip resistance for slip system α, respectively. The resolved shear stress is defined as:

$$\tau^\alpha = \left(\boldsymbol{F}^{\mathrm{eT}}\boldsymbol{F}^{\mathrm{e}}\boldsymbol{T}\right) : \left(\boldsymbol{m}_0^\alpha \otimes \boldsymbol{n}_0^\alpha\right) \approx \boldsymbol{T} : \left(\boldsymbol{m}_0^\alpha \otimes \boldsymbol{n}_0^\alpha\right), \quad (4)$$

where $\boldsymbol{T}$ is the second Piola-Kirchoff (PK2) stress. As in Kalidindi et al,[38] the resolved shear stress is approximated by neglecting the effect of elastic stretching. The PK2 stress is defined as

$$\boldsymbol{T} = \frac{1}{2}\mathcal{L} \cdot \left(\boldsymbol{F}^{\mathrm{eT}}\boldsymbol{F}^{\mathrm{e}} - \boldsymbol{I}\right), \quad (5)$$

where $\mathcal{L}$ is the fourth-order elasticity tensor. Finally, the Cauchy stress, $\boldsymbol{\sigma}$, can be calculated from the PK2 stress:

$$\boldsymbol{\sigma} = \boldsymbol{F}^{\mathrm{e}}\left(\frac{1}{\det(\boldsymbol{F}^{\mathrm{e}})}\boldsymbol{T}\right)\boldsymbol{F}^{\mathrm{eT}}. \quad (6)$$

The model uses isotropic hardening to evolve slip resistance on slip system α, which follows Yaghoobi et al.[39]:

$$\dot{s}^\alpha = \sum_\beta h^{\alpha\beta}\dot{\gamma}^\beta, \quad (7)$$

where $h^{\alpha\beta}$ is a hardening modulus on slip system α due to the slip rate on slip system β. The hardening moduli are defined as

$$h^{\alpha\beta} = \begin{cases} h_0^\beta \left[1 - \frac{s^\beta}{s_s^\beta}\right]^{a^\beta}, & \text{if } \alpha = \beta \\ h_0^\beta q \left[1 - \frac{s^\beta}{s_s^\beta}\right]^{a^\beta}, & \text{if } \alpha \neq \beta \end{cases} \quad (8)$$

where q is the latent hardening ratio, h_0^β is the hardening parameter for slip system β, s_s^β is the slip resistance at hardening saturation for slip system β, and a^α is the hardening moduli's slip-resistance sensitivity. The constitutive model was calibrated using the stress-strain data for underaged (4-h) magnesium WE43 from Ganesan et al.[40] The calibration procedure from Ganesan et al[40] was performed with a rate-independent crystal plasticity model implemented in PRISMS-Plasticity[39,41]; additional details regarding the calibration are provided in Appendix B. The calibrated parameters from the rate-independent model were transferred directly to the rate-dependent model described above, although manual adjustment of m and $\dot{\gamma}_0$ was performed. Hexagonal-close packed basal, prismatic, and pyramidal slip systems are modeled. The elastic constants are taken from Githens et al[42] and Ganesan et al,[40] where $C_{11} = 59.3$, $C_{12} = 25.7$, $C_{13} = 21.4$, $C_{33} = 61.5$, and $C_{55} = 16.4$ MPa. The calibrated plastic parameters are provided in Table 1. The reference slip rate, $\dot{\gamma}_0$, and the strain-rate sensitivity parameter, m, are assumed to be constant for all slip systems. They are taken to be $\dot{\gamma}_0 = 0.001\,\mathrm{s}^{-1}$ and $m = 0.1$.

2.3 | Direct replication of known crack surfaces in thin-foil samples

To assess candidate crack-deflection criteria, the as-measured crack surfaces in the three thin-foil samples described in Section 2.1.1 were directly replicated (i.e., crack propagation was not predicted) and analyzed using high-fidelity FE models.

2.3.1 | Crack-path truncation methodology

Among the three thin-foil samples, 20 FE simulations were performed, where each simulation corresponded to a specific snapshot during the history of the crack surface in a given foil sample. The snapshots were created by simply truncating the crack surfaces along planes of interest in each foil, depicted in Figure 4A. Crack surfaces from the initiation location up to the different truncation planes were then modeled in independent FE simulations. Crack-truncation planes were selected to capture a variety of crack-growth characteristics, including primarily transgranular growth, primarily intergranular growth, and mixed conditions, as indicated in Figure 4A. Results from the 20 simulations were then used to assess candidate crack-deflection criteria by comparing calculated kink angles immediately ahead of the modeled crack front to the known kink angles for the corresponding set of points on the crack surface.

TABLE 1 Calibrated slip resistance and hardening parameters for underaged WE43.

Slip System	s_0^α (MPa)	h_0^α (MPa)	s_s^α (MPa)	a^β
Basal	40	595	90	2.5
Prismatic	85	412	170	2.5
Pyramidal<a>	95	373	195	2.5
Pyramidal<c+a>	115	321	205	2.5

2.3.2 | Model and mesh descriptions

In some regions of the foil samples, the experimental crack surfaces fall very near the boundaries (e.g., x-y planes) of the experimentally characterized microstructure, as shown in Figure 4A. To avoid boundary effects in the models, the microstructures are mirrored about the x-y planes above and below the crack surfaces and the vertical plane opposite the notched side of each foil. Figure 4B provides an example of a meshed foil model, where the original boundaries of the experimentally characterized microstructure are highlighted, and the microstructure is mirrored about the highlighted planes. The foils are effectively expanded by 30% in each direction for foil 2 and 40% in each direction for foils 1 and 3.

All simulations are run with 10-node quadratic tetrahedral elements. Using the mesh-gradation framework described in Section 2.2.1, the mesh is refined near the crack front and coarsened in the far field. The refinement region is approximately 112 μm in diameter, centered around the crack front, as depicted in Figure 4B. Elements near the crack front have an approximate nominal edge length of 2 μm, while elements in the far-field have an approximate nominal edge length of 16 μm, which are smaller than the minimum required element size to achieve mesh convergence (reported in Appendix A).

2.3.3 | Thin-foil sample boundary conditions

Foil sample models were loaded in displacement-control to a maximum nominal stress of approximately 60 MPa, as shown in Figure 4B. Nodes along the bottom surface were fixed in all directions, while nodes along the top surface were fixed in the x and y directions. Vertical displacement corresponding to a nominal applied stress of 60 MPa in an uncracked foil was applied along the top surface in each simulation. For all simulations, a single cycle was simulated by unloading to achieve a nominal

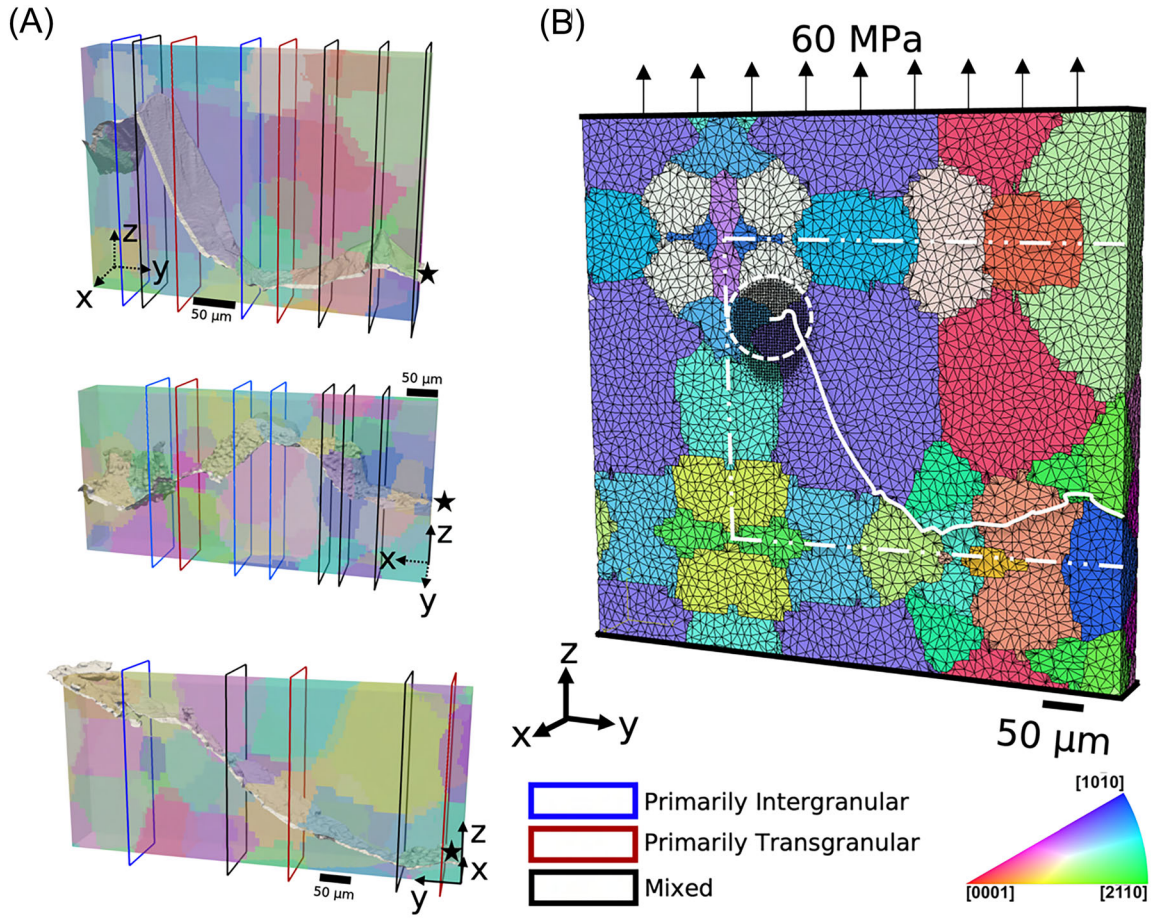

FIGURE 4 (A) Crack-truncation planes selected for the foil-sample models. Crack surfaces up to the different truncation planes were modeled in independent simulations to assess candidate crack-deflection criteria by comparing calculated to known crack deflection. Crack-truncation planes were selected to represent a variety of different crack-growth characteristics: primarily intergranular, primarily transgranular, and mixed conditions. Star indicates crack initiation locations. (B) Typical mesh and boundary conditions applied to the thin-foil sample simulations. The mesh is refined near the crack front (white circle) and coarsened in the far field. The crack is outlined in white. The microstructure was mirrored about the boundaries of the experimentally measured microstructure (dotted-dashed line) to effectively expand the modeled microstructure in the y-z plane. Nodes are fixed in all directions on the bottom surface and in the x and y directions on the top surface. A nominal vertical displacement corresponding to 60 MPa in the uncracked microstructure is applied on the top surface prior to unloading with $R = 0.1$ [Colour figure can be viewed at wileyonlinelibrary.com]

load ratio of $R = 0.1$; it was found that additional cycles did not significantly affect the kink-angle predictions, which is similar to findings reported in the literature.[25,28,43]

2.3.4 | Selected crack-deflection criteria

Three criteria for crack growth direction are investigated in this work: the maximum tangential stress (MTS) criterion,[44] a FIP based on work by Fatemi and Socie,[19] and the spatial gradient of the Fatemi-Socie-based FIP. Each criterion is evaluated by probing relevant field variables along the probe path, Φ (see Figure 3D), at each point along the crack front in a given snapshot, or crack-truncation, simulation. Criteria are evaluated at the peak of the final simulated loading cycle (i.e., in tension).[‡] The probe-path radius, R_p, is 10 μm, which is comparable to probe radii used in similar studies in the literature.[24,28] Further, R_p values ranging from 5 μm to 30 μm were tested, and no significant difference was found in the relative field-variable peaks.

Maximum tangential stress criterion

The MTS criterion[44] asserts that crack growth occurs in the direction that maximizes local opening stress

[‡]Preliminary testing showed that evaluating crack-deflection criteria at either the peak applied load or over the complete range of cyclic loading yielded similar predictions.

(i.e., Mode I) and is commonly used for predicting crack-growth direction at the macroscale. In heterogeneous or anisotropic materials, the local stress state can be influenced by the local material constituents, such that the local opening stress is not strictly perpendicular to the global loading direction. The MTS, or derivations thereof, have been used to study kink-angle in heterogeneous or anisotropic materials.[45–48] Zhang and Dunne[14] simulated short cracks across grain boundaries for various twist and tilt angles and found modest variation in the stress fields at the crack front when the crack-front impinges on a grain boundary with a large mismatching twist angle. In other work, Hochhalter et al[15] found that the local MTS correlated with short-crack nucleation direction.

The predicted kink-angle due to the MTS is defined here as

$$\phi_{MTS} = \arg\max_{\Phi}(\sigma_{\tan}[..]), \tag{9}$$

where $\sigma_{\tan}[..]$ indicates an array of tangential stress values evaluated along probe path Φ, and the operation $\arg\max_{\Phi}$ returns the kink angle ϕ that corresponds to the maximum value in the array.

Maximum Fatemi-Socie criterion

The second candidate crack-deflection criterion is a non-local damage parameter (i.e., FIP) based on work by Fatemi and Socie.[19] FIPs based on the Fatemi-Socie parameter have been used to assess short-crack growth rate/extension[20,21,49] and short-crack nucleation.[18] Rovinelli et al[27] reported a decent correlation between FIPs and an experimentally observed crack path in a volume of beta-titanium alloy. Furthermore, the Fatemi-Socie parameter has been used by Proudhon et al[28] for predicting crack-growth extension and deflection in the aforementioned experimentally characterized volume of beta-titanium alloy, but the crack-growth predictions informed by the Fatemi-Socie parameter were not directly compared to the observed crack path.

In this work, the maximum Fatemi-Socie (MFS) criterion is calculated as[18]

$$D = \max_{\mathrm{p}}\left[\int_0^t \sum_{\alpha=0}^{N_p} |\dot{\gamma}_p^{\alpha}|\left(1 + k\frac{\langle\sigma_n^p\rangle}{s_o^{\alpha}}\right)\mathrm{dt}\right], \tag{10}$$

where N_p is the number of slip systems on a single slip plane, $\langle\sigma_n^p\rangle$ is the tensile stress on slip plane p, k is a parameter that defines the relative influence of tensile stress and accumulated slip, and $\max_{\mathrm{p}}$ returns the maximum value across all slip planes. Equation (10) is evaluated at the integration points and probed according to the procedure outlined in Section 2.2.1. As in previous studies,[18,19] k is set to 0.5. The kink angle from MFS with no modifications, $\phi_{\max[D]}$, is defined as

$$\phi_{\max[D]} = \arg\max_{\Phi}(D[..]), \tag{11}$$

where $D[..]$ is an array of D values evaluated along probe path Φ. Equation (11) states that, at a given crack-front point, the crack will propagate in the direction of maximum D evaluated along probe path Φ.

Gradient of maximum Fatemi-Socie criterion

Pierson et al[25] found that the spatial gradient of FE simulation field variables yielded a higher correlation to the crack path than the variables themselves. Therefore, the spatial gradient of the MFS criterion, ∇D, is considered the final potential crack-deflection criterion. The kink angle from ∇D, with no modifications, can be written as

$$\phi_{\max[\nabla D]} = \arg\max_{\Phi}\left(\left|\frac{\partial D}{\partial \Phi}\right|[..]\right) = \arg\max_{\Phi}(\nabla D[..]), \tag{12}$$

where $\nabla D[..]$ is an array of $|\nabla D|$ values evaluated along probe path Φ. Unlike previous criteria, Equation (12) is not directly evaluated as a solution variable. Instead, it is calculated discretely along the probe path after the interpolated values of MFS have been returned using the path feature in ABAQUS,[36] as described in Section 2.2.1. Equation (12) states the crack will grow in the direction of maximum $|\nabla D|$ evaluated along probe path Φ.

2.3.5 | Graph-based selection of kink angle for slip-based criteria

In the preliminary analysis of the crack-deflection criteria, it was found that applying Equations (11) and (12) without modification yielded poor kink-angle predictions. Upon further investigation, the poor predictions were found to be related to multiple similar-valued peaks in the slip-based damage metrics along certain probe paths. To illustrate, Figure 5 shows a mixed-case truncated crack model in foil 2 and the corresponding predictions of kink angle evaluated along the crack front of the model. The dashed black line in the kink-angle plot corresponds to the predictions from Equation (11) along the crack front, and the experimentally observed kink angle measured at a distance of $R_p = 10$ μm from the crack front is plotted in gold. For each crack-front point, gray dots in the plot indicate positions along the probe path that correspond to the local maxima of D. Following the

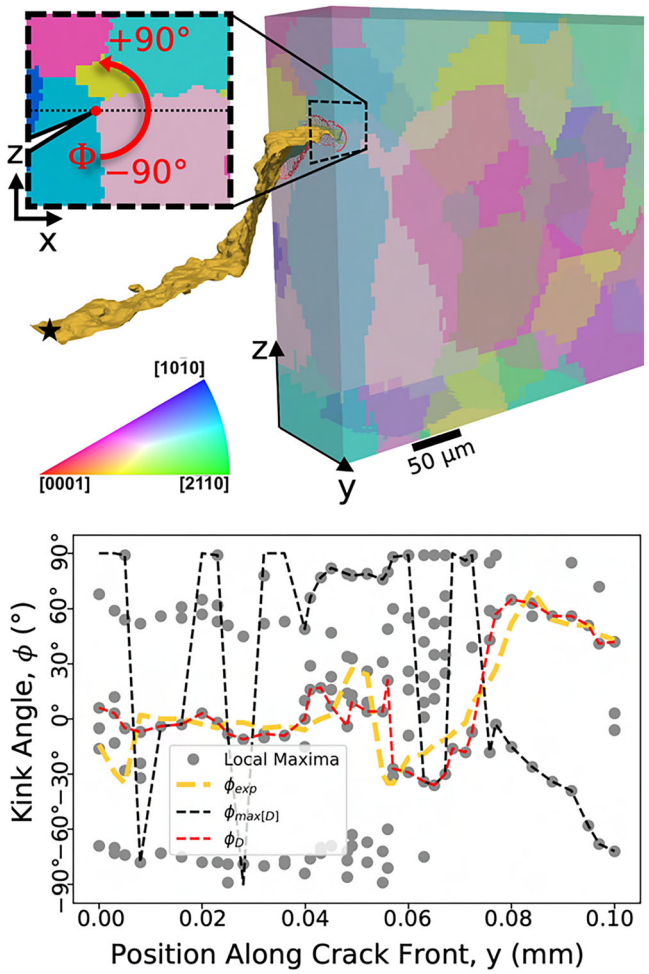

FIGURE 5 Foil simulation with depicted crack in foil 2. Illustration on top shows the cracked surface, and the remaining uncracked microstructure. Star indicates the approximate crack initiation location. Plot on the bottom shows the predicted kink angle from the absolute maximum D value along a probe path ($\phi_{\max[D]}$), local maxima along each probe path, the experimentally observed kink angle, and the predicted kink angle based on D after application of the graph-based selection method (ϕ_D) [Colour figure can be viewed at wileyonlinelibrary.com]

gold curve in the plot, it can be seen that there exist local maxima that correlate with the experimental kink angle. Therefore, a robust method is needed to select a local maximum from the set of peaks (local maxima).

A graph-based approach is proposed, in which the peaks of the damage metrics are represented with a graph structure, and the shortest path through the graph (after applying edge weighting) is used to select the kink angles along the crack front. For the example provided in Figure 5, the resulting graph-based predictions using computed D values result in the kink-angle predictions along the dashed red line, which matches more closely the experimentally observed kink angles. Details regarding the implementation are provided next.

A graph in computer science is a common abstract datatype that consists of nodes and edges, where nodes are connected by a series of edges and can be used to model the relationships between the nodes. Here, nodes are defined as locations of peak damage metrics (i.e., potential predicted kink angles), and the peaks from one probe path are connected to the peaks in the next probe path via edges. Figure 6 illustrates the overall graph methodology. Figure 6A represents a cracked microstructure, with four semi-circular probes along the crack front, x. A detailed view of the plane containing one crack-front point is shown in Figure 6B, where the probe path, Φ, is shown in red. Two potential peaks, which correspond to the local maxima of an arbitrary field variable, κ (viz., D or $|\nabla D|$), are marked as ϕ_2 and ϕ_3. Figure 6C shows the raw field variables resulting from each probe path, where probe path 2 (plotted in red) corresponds to the probe path illustration in Figure 6B. Note the two local maxima corresponding to ϕ_2 and ϕ_3. Local maxima are marked with dotted lines. These local maxima are considered nodes in the graph, shown in Figure 6D. Two auxiliary end nodes (0 and N) are inserted to enable the use of graph-based algorithms (described next). With the potential peaks represented in the graph, the edges between the peaks are weighted as follows:

Edge weighting based on Euclidean distance between peaks

Large variations in kink angles between neighboring points along the crack front are not realistic. To minimize large kink-angle variations along the crack front, the graph edges are weighted by the Euclidean distances between connected nodes. Figure 6B illustrates the spatial positions of peaks 2 and 3 as p_2 and p_3, respectively. Figure 6D shows the edges weighted by distance, where $d_{1,2}$ is the Euclidean distance between p_1 (not illustrated) and p_2, and $d_{1,3}$ is the Euclidean distance between p_1 (not illustrated) and p_3. This weighting is performed similarly for all edges in the graph. To eliminate bias from the end nodes, the distances from the end nodes to adjacent peaks are set to a constant distance, d_c.

Edge weighting based on relative peak magnitude

The magnitudes of each peak in the κ field are accounted for by multiplying the distances, $d_{i,j}$, by a weighting factor $\eta^1_{i,j}$ defined as:

$$\eta^1_{i,j} = 1 - a_1 \frac{\kappa_j}{\max[\kappa[..]]}, \tag{13}$$

where a_1 is a user-specified parameter, κ_j is the field-variable magnitude associated with node j, and $\kappa[..]$ is an

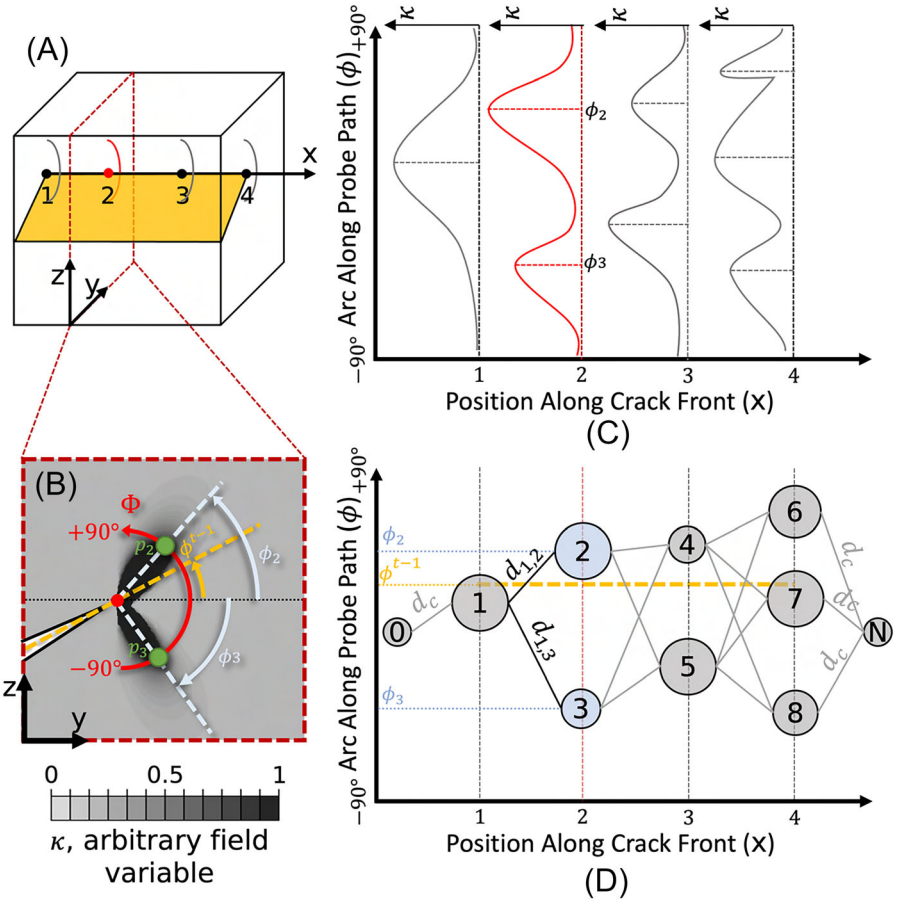

FIGURE 6 Overview of the graph-based approach to select local kink angles based on FIP fields, represented arbitrarily as κ. (A) Crack surface (gold) in microstructure, with semi-circular probes ahead of discrete crack-front points. (B) Detailed view of probe plane for one specific crack-front point. Two potential peaks corresponding to local maxima of field variable κ are marked as ϕ_2 and ϕ_3 along the probe path, Φ. Current crack orientation, ϕ^{t-1}, is marked in gold. (C) Distributions of field variable κ along probe paths for the discrete crack-front points depicted in (A). (D) Graph representation, where graph nodes correspond to peaks in κ with size indicating the relative magnitude of each peak. Edges are weighted by relative magnitudes of κ peaks for connected nodes and by angular mismatch (or similarity) with the current crack inclination angle. [Colour figure can be viewed at wileyonlinelibrary.com]

array of field-variable magnitudes along the probe path of the crack-front point containing node j. In this equation, edges that connect to a peak with a larger magnitude are shortened and, therefore, more favorable to be selected by the shortest-path algorithm. The nature of this weighting is linear, and the influence of this weighting is set by the parameter a_1. The allowable domain for a_1 is [0,1); a value of $a_1 = 0$ ignores peak magnitude in the graph, and a value of $a_1 = 1$ generates a graph for which the shortest distance is undefined.

Edge weighting based on current crack orientation

It is well known in the literature that short-crack propagation is influenced by the local crack inclination angle and the surrounding microstructural features.[50] Large geometric incompatibilities between the crack geometry (e.g., inclination angle) and available slip systems or grain boundaries for propagation have been correlated with a reduction in crack growth rate or crack arrest.[6,51] Geometric incompatibilities are considered in the graph by weighting edges by the angular mismatch (in radians) between the current crack orientation, ϕ^{t-1}, and the predicted kink angle corresponding to node j, as illustrated in Figure 6B. This weight factor is defined as:

$$\eta_{i,j}^2 = a_2 + \frac{4}{\pi}(1-a_2)|\phi_j - \phi^{t-1}|, \tag{14}$$

where a_2 is a user-specified parameter and ϕ^{t-1} is evaluated at a distance R_p behind the crack front. The weighting factor is $\eta_{i,j}^2 = 1$ (no weighting is applied) when $|\phi_j - \phi^{t-1}| = 90°$, and $\eta_{i,j}^2 > 1$ (the edge is penalized) when $|\phi_j - \phi^{t-1}| > 90°$. The allowable domain for a_1 is [0,1].

The final edge weight assigned to each edge is defined as:

$$d_{i,j}^{\text{final}} = \eta_{i,j}^1 \eta_{i,j}^2 d_{i,j}, \tag{15}$$

and the final kink angles along the crack front are comprised of the peaks associated with the shortest path from node 0 to node N.

The influence of the weighting factors is tuned by user constants a_1 and a_2. To determine reasonable factors to use, the L2-error norm was minimized between kink-angle predictions and experimentally observed kink angles for all crack-front points in the 20 snapshot simulations described in Section 2.3.1. Values for a_1 and a_2 in the range of [0,1) were tested in 0.1 increments. The weighting parameter values that produced the lowest L2-error norm are $a_1 = 0.0$ and $a_1 = 0.2$ for the D and ∇D

criteria, respectively, and $a_2 = 0.8$ for both D and ∇D criteria. With the tuned parameters, the predicted kink-angle based on D is defined as

$$\phi_D = G(D), \tag{16}$$

where $G(D)$ represents the kink-angle after applying the graph-based operation on $D[..]$ for all crack-front points. The red line in Figure 5 shows the predicted kink angle based on D after applying the graph-based method. Similarly, the predicted kink-angle based on ∇D with the graph-based method applied is defined as:

$$\phi_{\nabla D} = G(\nabla D). \tag{17}$$

2.4 | Blind predictions in WE43 cylindrical sample

Using the crack-deflection criteria developed in the previous section, blind predictions of the three-dimensional crack path were performed in the polycrystalline volume extracted from the cylindrical fatigue sample described in Section 2.1.

2.4.1 | Initial crack insertion and meshing

An initial semi-circular crack with approximate dimension $2a = 90$ μm was inserted along the basal plane of the initiation grain as shown in Figure 7B,C. Using the mesh-gradation framework described in Section 2.2.1, the mesh was refined near the crack front and coarsened in the far-field. The refinement region was approximately 60 μm in diameter and tracks with the evolving crack front. Elements near the crack front had an approximate nominal edge length of 2.1 μm, while elements in the far-field had an approximate nominal edge length between 21 μm and 33 μm, which were smaller than the minimum required element size to achieve mesh convergence (reported in Appendix A). An example mesh is shown in Figure 7D.

2.4.2 | Boundary conditions

A submodeling approach was applied to the cracked polycrystal, as shown in Figure 7A–C. The full cylindrical sample was modeled using a simple elastic-plastic constitutive material, and one complete loading cycle (load, unload, and reload to peak load) was simulated with a maximum nominal stress of 85 MPa and $R = -1$. The complete loading cycle was then simulated on the

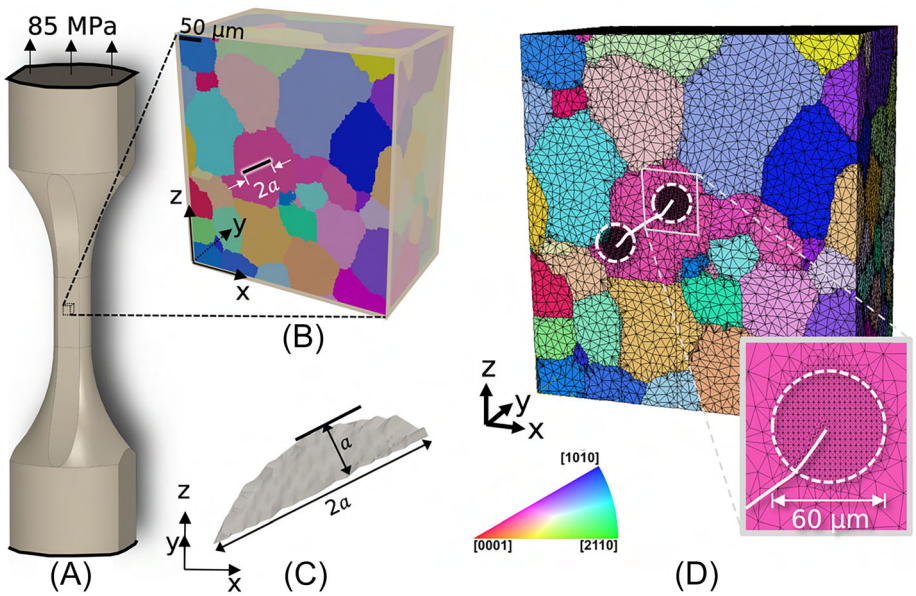

FIGURE 7 (A) Global geometry of cylindrical fatigue specimen used for submodeling, modeled with a simple elastic-plastic constitutive model and cycled for a single loading cycle to a nominal maximum stress of 85 MPa and $R = -1$. (B) Interpolated displacements from the global model are applied to faces of the polycrystalline model (including the y+ face, which is not visible). Interpolated displacements are not applied on the y- face (which is a free surface). (C) Magnified view of the inserted crack surface, where $2a = 90$ μm. (D) An example mesh for the three-dimensional cracked polycrystal, where the crack is depicted as a solid white line. The refinement region is approximately 60 μm in diameter, centered around the crack front, depicted with dotted lines. The local mesh has an approximate nominal edge length of 2.1 μm. The global approximate nominal edge length in this model is 21 μm. [Colour figure can be viewed at wileyonlinelibrary.com]

polycrystal (for each crack-growth increment) by applying the interpolated displacements from the global model to the faces of the polycrystalline model except the y-face, as depicted in Figure 7B.

2.4.3 | Crack-evolution criteria

The three candidate deflection criteria are assessed by performing three separate crack-growth simulations using the crack-simulation framework described in Section 2.2.1. At the second peak applied load for each crack increment, field variables are extracted ahead of each crack-front point along a probe path of radius $R_p = 10$ μm. The field variables are then used to assess subsequent crack growth at each crack-front point according to the criteria described in Section 2.3.4. As this work is focused on evaluating crack-deflection criteria, crack extension is defined to be uniform along the crack front with a value of $da = 30$ μm. This value was selected to balance computational expense and crack-path resolution with respect to grain size; specifically, approximately three crack-growth increments would occur in each grain based on an average grain size of 113 μm reported for the material.[8]

3 | RESULTS AND DISCUSSION

3.1 | Results from direct replication of crack surfaces in thin-foil samples

Contour plots of the L2-error norm from the graph calibration are shown in Figure 8. Figure 8A is the $G(D)$ L2-error norm contour for different values of a_1 and a_2, and Figure 8B is the $G(\nabla D)$ L2-error norm contour. The parameter values which produced the lowest L2-error norm, as described in Section 2.3.5, are marked with an X in Figure 8. As seen in the contour plots, using parameter values that effectively disable weighting ($a_1 = 0$, $a_2 = 1$) produces poor predictions. These observations suggest that weighting provides tangible benefits. Conversely, applying the maximum weighting ($a_1 \approx 1$, $a_2 = 0$) also produces poor results. Rather, for both slip-based criteria, there exists a region in the space of weighting-parameter values that provides similar accuracy to that obtained using the values which produced the lowest L2-error norm. Furthermore, the overall L2-error norms indicate that $G(\nabla D)$ produces kink angles closer to those observed in the experimental crack surface than those produced by $G(D)$, which agrees with the findings in Pierson et al.[25]

In Figure 9, the predicted and experimental kink angles from the three criteria are displayed for one

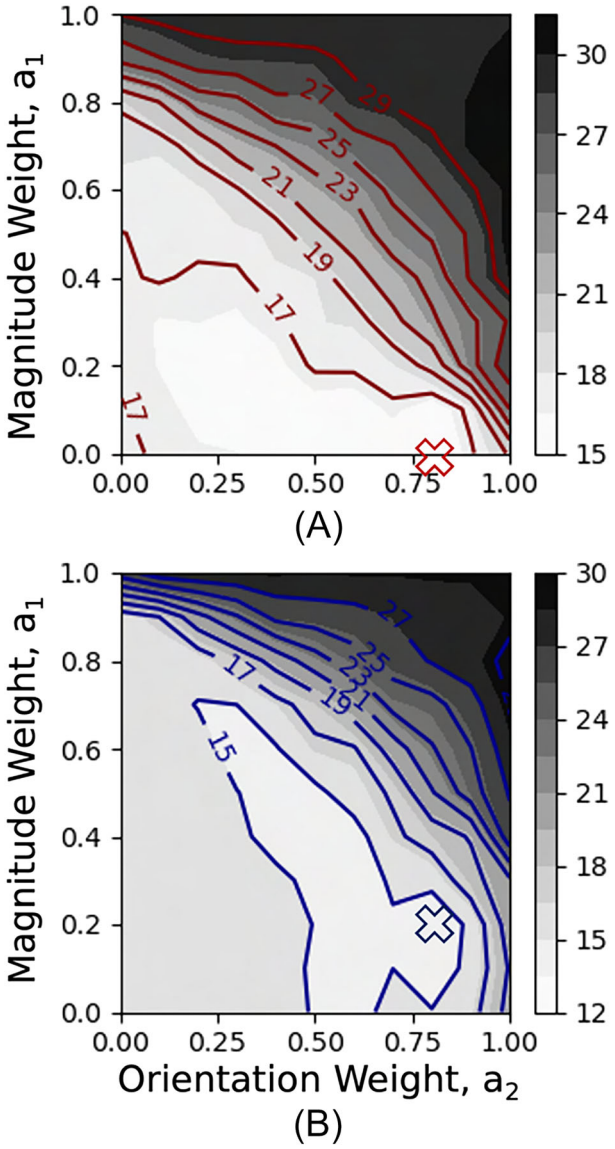

FIGURE 8 Contour plots of L2 error norm from the graph calibration from Section 2.3.5. (A) L2 error norm contour for $\phi_D = G(D[..])$. (B) L2 error norm contour for $\phi_{\nabla D} = G(\nabla D[..])$. In each contour plot, X denotes the values of a_1 and a_2 resulting in the lowest error. [Colour figure can be viewed at wileyonlinelibrary.com]

representative snapshot in each foil. Results for a transgranular (A), intergranular (B), and mixed case (C) are shown. The left column of Figure 9 shows truncated views of the experimental crack surface (depicted in gold), grains adjacent to the experimental crack surface, and probe paths along each crack front. The right column shows the kink-angle predictions from the three criteria and the experimentally observed kink angle along the crack fronts. In Figure 9A,B, the prediction from $G(\nabla D)$ is closer to the experimentally observed kink angle than that from $G(D)$. There are cases where neither slip-based

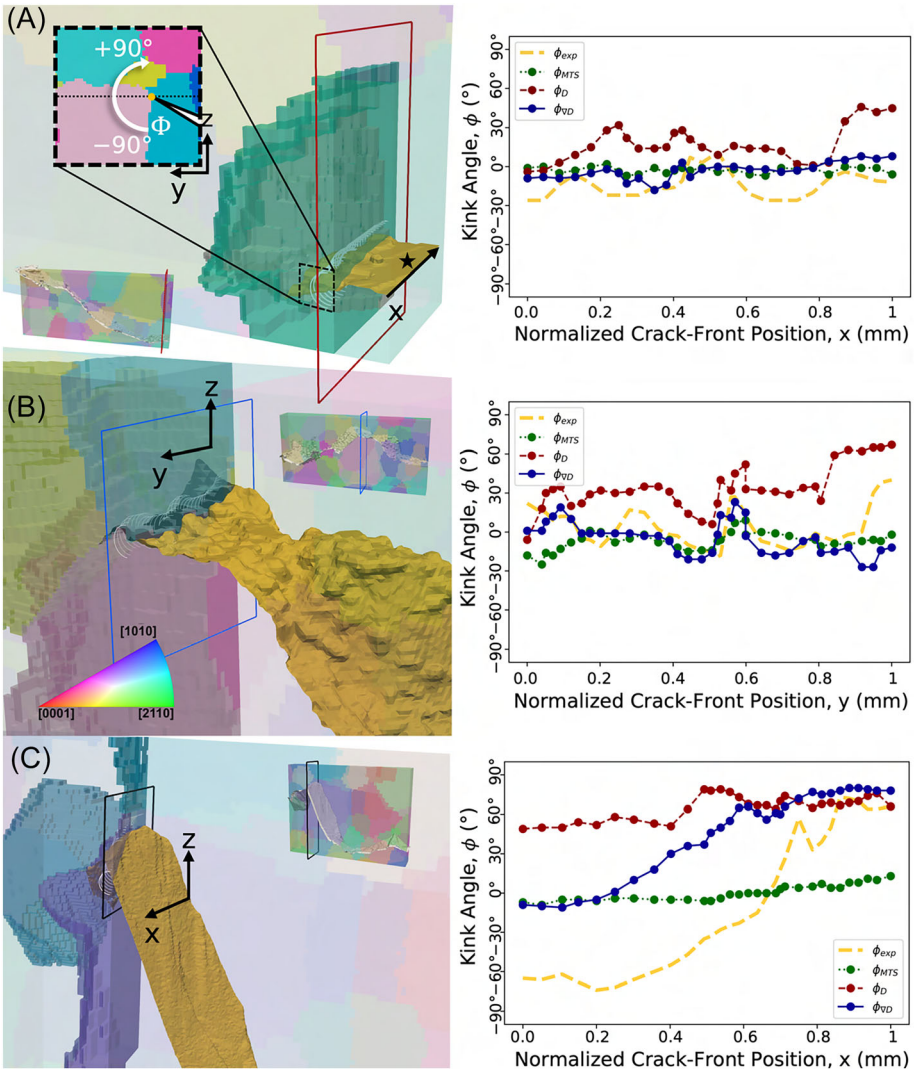

FIGURE 9 Selected cases of the predicted and experimental kink angles for each foil: (A) transgranular growth in foil 3, where star indicates initiation location; (B) intergranular growth in foil 2; and (C) mixed case in foil 1. Left column shows magnified views of the truncated experimental crack surface (i.e., snapshot), grains adjacent to experimental crack surface, and probe paths. Right column shows the kink-angle predictions from the three criteria (MTS, $G(D)$, and $G(\nabla D)$) and the experimentally observed kink angles along each crack front. Note that a different through-thickness axis orientation is used in (B) due to a different experimental reference system compared to (A) and (C). [Colour figure can be viewed at wileyonlinelibrary.com]

criterion can predict the experimentally observed kink angle, as shown in Figure 9C; in these cases, the slip-based criteria fail to predict the correct kink angle since the experimental crack surface exhibits significant deflection, which is penalized with orientation weighting. While there are minor variations in the kink-angle predictions along the crack front based on the MTS criterion, the predicted kink angles remain predominantly orthogonal to the loading direction. This behavior is especially evident in Figure 9C, for which the MTS criterion predicts crack growth perpendicular to the loading direction, despite this not being the case in the experiment.

3.2 | Results from blind prediction in three-dimensional WE43 polycrystal

In total, 22 FE analyses with crystal plasticity and one complete loading cycle each were performed to make the blind predictions described in Section 2.4. In addition to one FE analysis corresponding to the initial crack, seven crack-growth increments were simulated for each of the three crack-deflection criteria. Blind-prediction simulations used an approximate cumulative 66200 CPU hours to complete on a combination of Intel XeonSP Skylake, Intel XeonSP Cascade Lake, and AMD Rome CPUs at the University of Utah Center for High-Performance Computing.

Figure 10 shows the crack-surface prediction informed by the MTS criterion, colored by the elevation error (ΔZ), which is simply the difference between the predicted and observed elevation of the crack surface at a given (x,y) location. Figure 11 shows the same plots for the crack-surface predictions informed by the two slip-based criteria, $G(D)$ and $G(\nabla D)$, shown from multiple views. Blue indicates the predicted crack surface is below the experimentally observed crack surface, while red indicates the predicted crack surface is above the experimentally observed crack surface. The experimental crack surface is shown as a black wire frame. Projected views

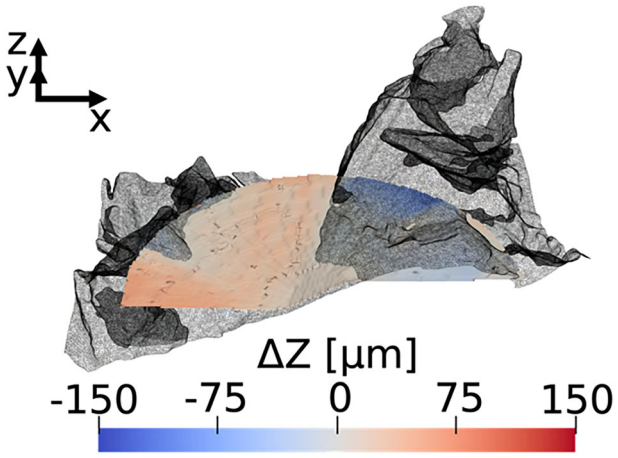

FIGURE 10 Predicted three-dimensional crack surface informed by the MTS criterion, colored by elevation error relative to the experimental crack surface (ΔZ); the experimentally observed crack surface is shown as a black wire frame. [Colour figure can be viewed at wileyonlinelibrary.com]

of the predicted crack surfaces based on all three crack-deflection criteria are shown in Figure 12. The left column is colored by the elevation error (ΔZ). The right column is colored by the error in the surface normal (ΔN), which is the difference between the predicted and observed crack-surface normal at a given (x,y) location. Portions of the predicted crack surface colored in white indicate good agreement, while portions in black have poor agreement.

Frequency distributions of the error metrics ($|\Delta Z|$ and ΔN) over the entire predicted crack surfaces are presented in Figure 13 for the MTS criterion (A), $G(D)$ criterion (B), and $G(\nabla D)$ criterion (C). Crack traces along specific planes of interest are shown in Figure 14 for the experimentally observed crack surface and the crack surfaces predicted by the three crack-deflection criteria.

Based on the mean and standard deviation of the error metrics ($|\Delta Z|$ and ΔN) shown in Figure 13 and on the visual comparison of color contours presented in

FIGURE 11 Predicted three-dimensional crack surfaces informed by the slip-based criteria, colored by elevation error relative to the experimental crack surface (ΔZ); the experimentally observed crack surface is shown as a black wire frame. [Colour figure can be viewed at wileyonlinelibrary.com]

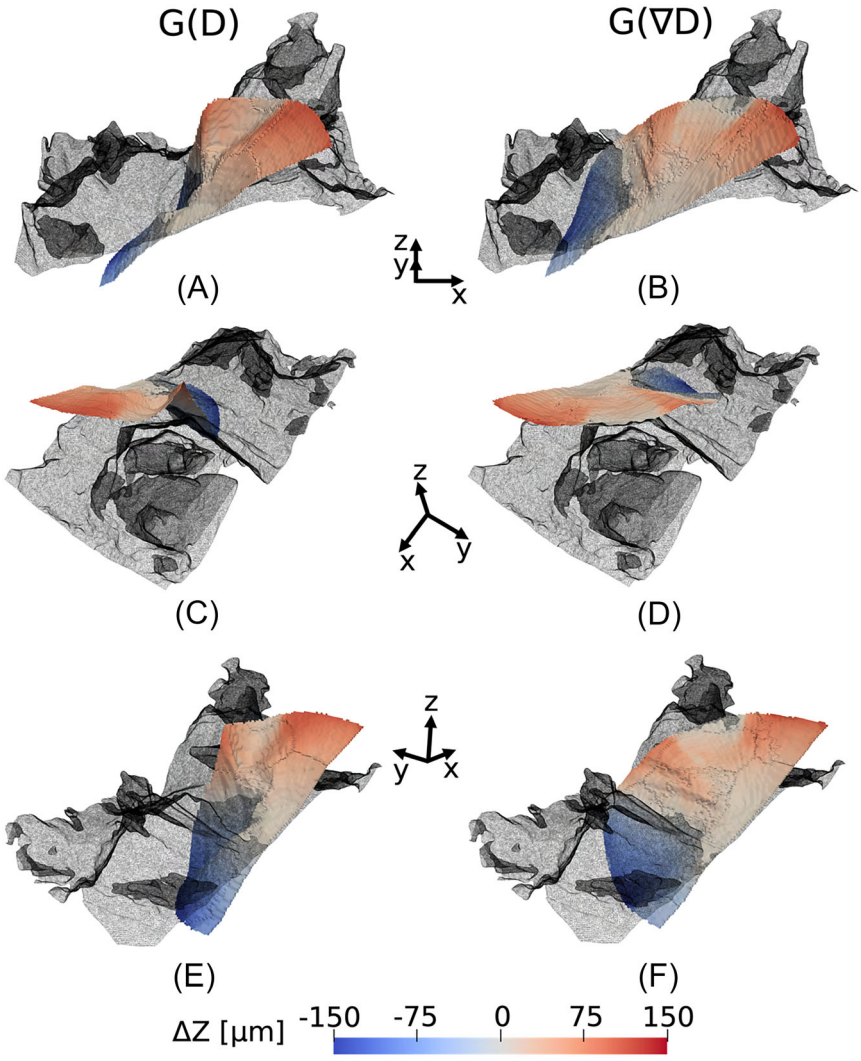

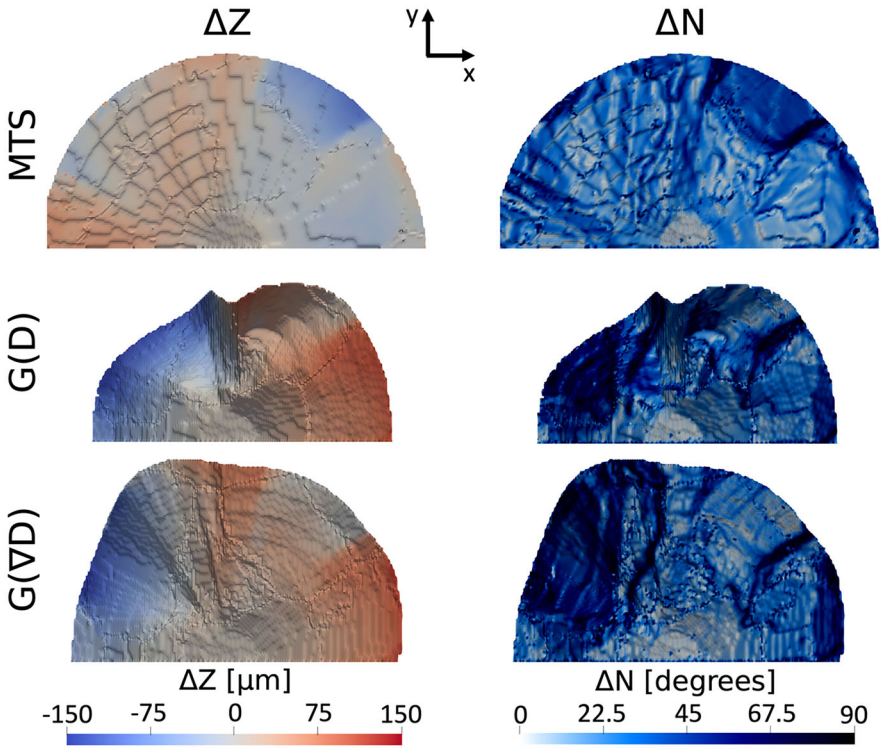

FIGURE 12 Projected view on the x-y plane for the predicted crack surfaces from all three crack-deflection criteria. Elevation error (ΔZ) is shown in the left column, where blue and red indicate crack-surface predictions below and above, respectively, the experimentally observed crack surface. Surface-normal error (ΔN) is shown in the right column. [Colour figure can be viewed at wileyonlinelibrary.com]

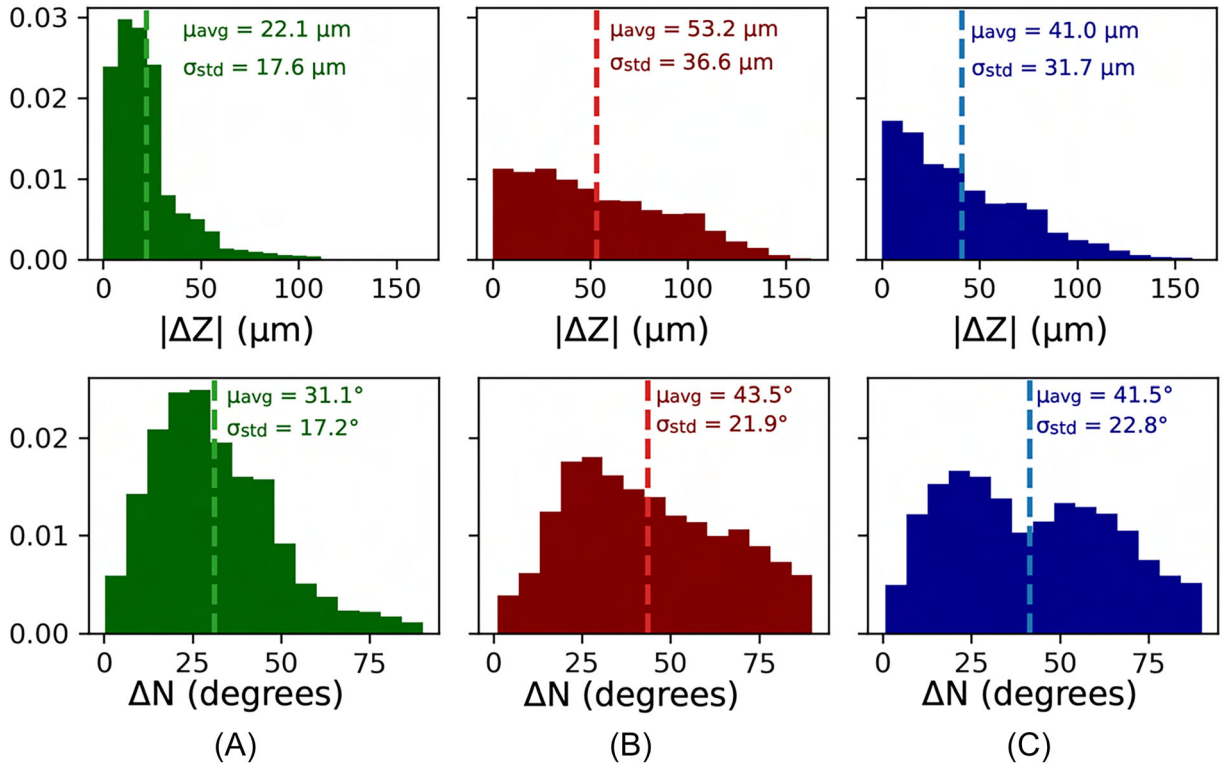

FIGURE 13 Histograms of the absolute-elevation and surface-normal errors between the predicted crack surfaces and the experimental crack surface for each crack-deflection criterion considered: (A) MTS, (B) $G(D)$, and (C) $G(\nabla D)$ [Colour figure can be viewed at wileyonlinelibrary.com]

Figure 12, the MTS criterion appears to perform quantitatively better than the two slip-based criteria. This apparent performance is attributed to the fact that the predicted kink angles from the MTS criterion remain nominally orthogonal to the global loading direction with little crack deflection along the crack surface, thereby

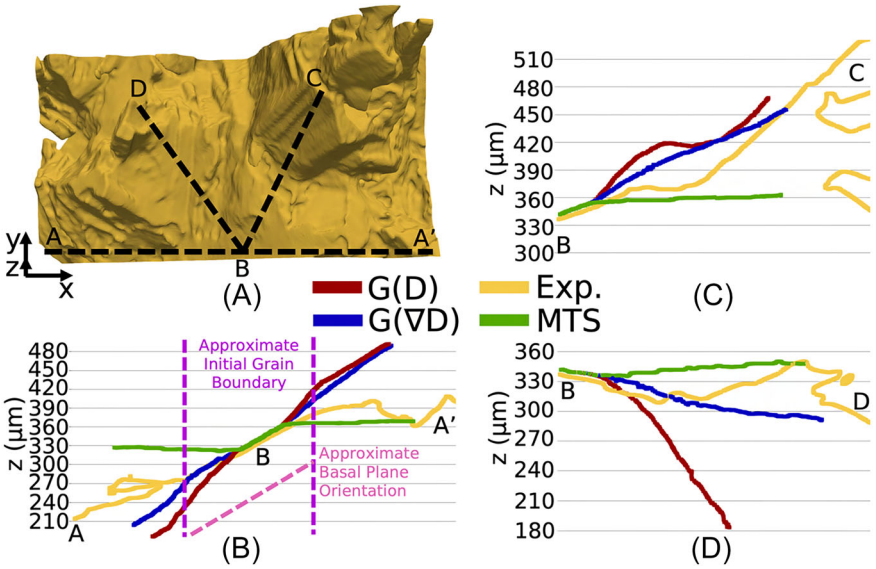

FIGURE 14 Comparisons between predicted and experimental crack traces: (A) experimental crack surface depicting the reference lines of interest, (B) crack traces along A–A′, (C) crack traces along B–C, (D) crack traces along B–D. [Colour figure can be viewed at wileyonlinelibrary.com]

capturing an average behavior of the experimentally observed crack surface. This is especially evident in the crack traces shown in Figure 14. Thus, it is clear that the predicted crack surface from the MTS criterion is not significantly affected by the local microstructure. Despite the apparent superiority of the error metrics from the predictions based on the MTS criterion (for the simulated material, assumptions, and boundary conditions), the relative insensitivity to the local microstructure limits the potential utility of the MTS criterion for predicting short-crack behavior (discussed later).

The overall elevation error for the crack surface predicted by $G(D)$ is the highest among the three criteria considered, as quantified by the average and standard deviation values reported in the frequency plots of Figure 13. Despite this, the crack surface informed by $G(D)$ appears to exhibit the most sensitivity to the microstructure, as illustrated collectively in Figures 11–14. Interestingly, the angle corresponding to a local maximum of D does not necessarily coincide with the angle of orientation of a slip plane intersecting the crack front. This discrepancy is apparent in Figure 14B, where predictions from $G(D)$ deviate from the experimentally observed crystallographic crack growth along the basal plane. A similar discrepancy between the angle corresponding to a maximum value of a Fatemi-Socie-based parameter and specific slip plane has been reported for body-centered cubic single-crystal short-crack simulations where only a single slip system was modeled[23] and in later work where multiple slip systems were modeled in a single crystal.[24] While the current crack-growth implementation does not yield predictions that ideally match the experimentally observed crack surface, selected traces on the crack surface (e.g., Figure 14C) show that $G(D)$ qualitatively captures instances of crack-deflection in the experimentally observed crack surface. Therefore, it is reasonable to infer that slip-based metrics, such as the Fatemi-Socie[19] parameter and other FIPs, can potentially serve as predictors for short-crack path, but further investigation is needed to understand anomalous behavior and the specific criteria governing crack growth under the conditions studied here.

The overall elevation error for the predicted crack surface informed by $G(\nabla D)$ is smaller than that for $G(D)$, as shown in Figures 12 and 13. Upon closer inspection, the predicted crack surface based on $G(\nabla D)$ appears to grow self-similarly (Figure 11B). Hence, the reason for the apparent better performance is similar to that for the MTS criterion: the crack surface is capturing an average behavior. However, unlike the MTS criterion, which predicts a crack surface that is nominally orthogonal to the global loading direction, the crack surface predicted using the $G(\nabla D)$ criterion appears nominally to follow slip planes. Results from the thin-foil samples (viz., L2-norm trends, Figure 8B, and selected foil cases, Figure 9) suggest that there exist peaks in the distribution of ∇D that better align with kink angles along the experimental crack surface than peaks from D. This behavior may possibly be due to a physical phenomenon (e.g., the crack is more likely to follow a path along which the most intense localization) or ∇D may implicitly capture driving forces that are not explicitly modeled; these postulations will require further study. Regardless, the existence of the aforementioned peaks explains why the criterion based on ∇D initially outperforms the predictions based on D within the first grain of the crack surface. However, once the predicted crack surface exits the initial grain, the predictions based on ∇D do not exhibit

deflections as pronounced as those observed in the experimental crack surface or predicted by D.

A possible reason for the apparent self-similar growth in the $G(\nabla D)$ predictions is that the directly replicated thin-foil simulations, against which the weighting parameter values were calibrated, are heavily biased towards self-similar growth (Figure 4A). Furthermore, there are more peaks along the probe paths of ∇D than of D. Therefore, there might exist a bias in the graph-based algorithm towards peaks that are most compatible with the local orientation. In summary, although parameter values that produced the lowest L2-norm errors for the foil samples were used in the blind prediction, it is possible that a separate set of weighting parameters would produce improved results for the three-dimensional microstructure.

Although the overall elevation error metric suggests that the MTS criterion performs the best among the three criteria, the predictive capability of this rule is limited. For instance, the crack surface area for each prediction for a region shared by all three predicted crack surfaces in the x-y plane are 61,197 μm^3, 99,645 μm^3, and 78,085 μm^3 for the MTS, $G(D)$, and $G(\nabla D)$ criteria, respectively. The results indicate that for this region, the $G(D)$ prediction generated 63% more surface area than the MTS prediction. Although a constant extension was specified for blind predictions, the generated surface area is related to the predicted kink angles and has implications for accurately predicting the crack-growth rate. Figure 15 shows the average crack-growth rate in the x-y plane ($d\alpha$) for each simulated crack-growth increment. The $d\alpha$ values show that assuming uniform extension, the lack of significant deflection in the predictions from MTS would result in MTS-based simulations reaching the bounds of a given microstructural domain earlier than the slip-based metrics, which could significantly underestimate stage-I (and thus, total) fatigue life of a structural component.

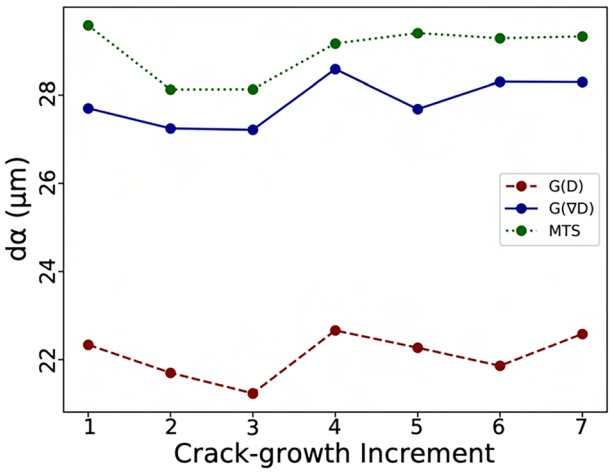

FIGURE 15 Average crack-growth rate in the x-y plane ($d\alpha$) for each simulated crack-growth increment. [Colour figure can be viewed at wileyonlinelibrary.com]

3.3 | Limitations and implications

While nf-HEDM and x-ray CT are currently considered state-of-the-art for experimentally characterizing three-dimensional microstructures and short-crack evolution, there are sources of uncertainty stemming from the experimental measurements that influence how the models are constructed and compared to the experiment. For example, not all microstructural features that might have influenced crack growth are represented in the experimental datasets; in particular, small grains and small sections of larger grains adjacent to the fracture surface may be omitted in the nf-HEDM reconstructions if the aforementioned regions of the microstructure fall between near-field line measurements or the diffraction peaks resulting from the small-lattice volumes are too faint to segment from background noise. Furthermore, limitations in access to beamtime (which influences how much volume can feasibly be measured), sample preparation, data resolution, and user decisions during data reconstruction also might have resulted in the inadvertent omission of influential grains in the models, for which interpolation ("filling the gaps") and extrapolation (extending the volume) was necessary.

Several assumptions and simplifications were applied to the numerical models to enable computational tractability. For instance, the accumulated plasticity is not mapped from one crack-growth increment to the next. Also, crack-face contact is not included in these simulations. Consequently, plasticity- and roughness-induced crack closure effects are not captured in the current work. Furthermore, the crack path is history-dependent, so errors early in the predictions can propagate and affect the final predicted fracture surface, as shown in Figure 14D. This could be alleviated by taking shorter nominal growth increments, da, but the computational expense would be significantly higher. Additionally, because this work is focused on the crack path, the crack-growth rate is treated as constant in the direction of crack deflection, which could affect predictions. Finally, not all mechanisms that potentially affect crack growth are included in the crystal-plasticity model. For instance, while isotropic hardening was assumed in this work, future work applied to cyclic loading may consider kinematic hardening (e.g., the Ohno-Wang hardening law[52] implemented in PRISMS-Fatigue[17]). Additional mechanisms such as backstress and dislocation substructure

development[53] could affect the driving force values extracted from the probe paths and are possible topics for future work. It is noted that large twins were not observed in the experimental dataset[30] and was, therefore, not included as a deformation mechanism in the constitutive model. Finally, while the crystal-plasticity calibration parameter values produce an admissible stress-strain response for an underaged WE43 alloy, the local strain fields produced by these parameter values have not been compared to experimental grain-level strain measurements. As such, uncertainty exists in the computed driving force that stems from the uncertainty in the calibrated crystal-plasticity parameter values. Quantifying the uncertainty in the driving force that results from various admissible sets of calibration parameter values is out of scope for this manuscript, but is a potential future topic of study.

This work primarily studies the driving force associated with short-crack propagation (viz., local deflection criteria), and crack-resisting forces are not explicitly considered. Future work using this framework could investigate the relationship between driving force, potential crack-resisting forces (e.g., misorientation at grain boundaries), and experimentally observed crack path. To obtain reasonable predictions without explicitly considering heterogeneous crack-resisting forces, the slip-based driving forces are influenced by a weighting factor that considers the geometric compatibility of a local crack orientation relative to a potential kink-angle. However, this approach is limited, where the current local crack orientation weighting implementation accounts for tilt but does not explicitly incorporate twist, which is an important factor in short-crack propagation.[7,14] This is a possible topic for future work.

Despite the above limitations, this work shows that FIPs such as the Fatemi-Socie parameter exhibit potential as predictors for crack deflection in underaged magnesium WE43 and that a graph-based representation of the FIP fields can assist with making reasonable predictions of deflection along three-dimensional crack fronts. The flexibility of the high-fidelity crack-simulation framework used in this study can be leveraged to assess different criteria, make additional modifications to the proposed criteria, or model different materials. Furthermore, while this work is focused on crack deflection, the framework's flexibility can also be used to assess criteria for crack-growth rate.

4 | CONCLUSION

A recently developed high-fidelity crack-simulation framework was used to model three-dimensional crack growth in experimentally measured microstructures of underaged magnesium WE43. Experimentally measured crack surfaces in three thin-foil samples were directly replicated to study candidate crack-deflection criteria by evaluating micromechanical fields ahead of the crack fronts at different times during the crack histories. Criteria based on the maximum tangential stress, a slip-based fatigue indicator parameter (FIP), and the spatial gradient of the slip-based FIP were considered. Because the slip-based criteria pose multiple possible deflection angles at a given crack-front point, a graph-based approach was implemented to aid in predicting kink angles along the three-dimensional crack fronts. The candidate crack-deflection criteria were then assessed by making blind predictions of three-dimensional crack propagation in an experimentally measured polycrystal extracted from a cylindrical fatigue specimen. The predicted crack surfaces were then compared to the experimentally measured crack surface to quantify relative performance among the candidate crack-deflection criteria. Based on the results, the following conclusions are drawn:

- While the maximum tangential stress criterion provides the lowest quantitative error measures among the three candidate criteria, the predicted crack surface remains relatively planar and nominally orthogonal to the global loading direction, thereby capturing an average elevation of the experimental crack surface without exhibiting observed sensitivity to local microstructure. Therefore, predictions from the maximum tangential stress criterion could significantly underestimate component fatigue life.
- The thin-foil assessments showed that spatial gradients of the FIP distributions could potentially produce accurate predictions. However, based on the blind predictions in the three-dimensional microstructure, the predictions informed by the spatial gradients of the FIP distributions produced a nearly self-similar crack surface nominally inclined along the initial crack geometry, indicating that additional modifications to the graph-based representation (e.g., weighting parameters) are required to obtain accurate predictions.
- Blind predictions based strictly on FIP distributions showed the most sensitivity to the local microstructure, despite being the least accurate quantitatively. This result suggests that, with additional modifications, FIP distributions can potentially be used as predictors for a short-crack path.
- Further investigation is needed to derive more accurate criteria for evaluating microstructurally small fatigue-crack evolution in underaged magnesium WE43. In addition to exploring different crack-driving

mechanisms, future efforts could consider anisotropic and heterogeneous crack-resisting mechanisms.
- The adaptive remeshing framework used in this work provides a powerful tool to assess user-specified criteria for three-dimensional crack propagation in heterogeneous microstructures.

AUTHOR CONTRIBUTIONS

Brian R. Phung: Conceptualization; methodology; software; investigation; writing—original draft; visualization. **Duncan A. Greeley**: Resources; data curation; methodology; writing—review and editing. **Mohammadreza Yaghoobi**: Software; resources; methodology; writing—review and editing. **Jacob F. Adams**: Resources; data curation; writing—review and editing. **John E. Allison**: Supervision; resources; project administration; writing—review and editing; funding acquisition. **Ashley D. Spear**: Supervision; resources; project administration; writing—review and editing; funding acquisition.

ACKNOWLEDGMENTS

This research was supported by the National Science Foundation under Grant Nos. CMMI-1629660 and CMMI-1752400. Experimental data collection was supported by the US Department of Energy, Office of Basic Energy Sciences, Division of Material Sciences and Engineering under Award No. DE-SC0008637 as part of the Center for PRedictive Integrated Structural Materials Science (PRISMS Center) at the University of Michigan. The authors would like to express gratitude to Junyan He and Kelly Clingo for their support for this work; Drs. Peter Kenesei and Hemant Sharma of the Advanced Photon Source, Argonne National Laboratory, for experimental assistance at beamline 1-ID and help with data reconstruction, respectively; Dr. Dillon Watring and Jayden Plumb for experimental assistance; and Bruce Davis of Magnesium Elektron for providing the materials for this research. The support and resources from the Center for High-Performance Computing at the University of Utah are gratefully acknowledged. This research used resources of the Advanced Photon Source, a U.S. Department of Energy (DOE) Office of Science user facility operated for the DOE Office of Science by Argonne National Laboratory under Contract No. DE-AC02-06CH11357.

CONFLICT OF INTEREST STATEMENT

The authors declare that they have no conflict of interest.

DATA AVAILABILITY STATEMENT

The data that support the findings of this study are available from the corresponding author upon reasonable request.

ORCID

Brian R. Phung https://orcid.org/0000-0003-0690-3115
Ashley D. Spear https://orcid.org/0000-0002-3933-3131

REFERENCES

1. Suresh S, Ritchie RO. Propagation of short fatigue cracks. *Int Met Rev*. 1984;29(6):445-475.
2. Hussain K. Short fatigue crack behaviour and analytical models: a review. *Eng Fract Mech*. 1997;58(4):327-354.
3. Paris P, Erdogan F. A critical analysis of crack propagation laws. *J Basic Eng*. 1963;85(4):528-533.
4. Castelluccio GM, McDowell DL. Assessment of small fatigue crack growth driving forces in single crystals with and without slip bands. *Int J Fract*. 2012;176(1):49-64.
5. Nicoletto G, Konečná R, Pirondi A. Fatigue crack paths in coarse-grained magnesium. *Fatigue Fract Eng Mater Struct*. 2005;28(1-2):237-244. _eprint: doi:10.1111/j.1460-2695.2004.00832.x
6. King A, Ludwig W, Herbig M, et al. Three-dimensional in situ observations of short fatigue crack growth in magnesium. *Acta Mater*. 2011;59(17):6761-6771.
7. Zhai T, Wilkinson AJ, Martin JW. A crystallographic mechanism for fatigue crack propagation through grain boundaries. *Acta Mater*. 2000;48(20):4917-4927.
8. Adams J. Investigating microstructural effects on short crack growth and fatigue life behavior of WE43 magnesium. Dissertation, University of Michigan.
9. Herbig M, King A, Reischig P, et al. 3-D growth of a short fatigue crack within a polycrystalline microstructure studied using combined diffraction and phase-contrast X-ray tomography. *Acta Mater*. 2011;59(2):590-601.
10. Schaef W, Marx M, Vehoff H, Heckl A, Randelzhofer P. A 3-D view on the mechanisms of short fatigue cracks interacting with grain boundaries. *Acta Mater*. 2011;59(5):1849-1861.
11. Spear AD, Li SF, Lind JF, Suter RM, Ingraffea AR. Three-dimensional characterization of microstructurally small fatigue-crack evolution using quantitative fractography combined with post-mortem X-ray tomography and high-energy X-ray diffraction microscopy. *Acta Mater*. 2014;76(413–424).
12. Rovinelli A, Lebensohn RA, Sangid MD. Influence of microstructure variability on short crack behavior through postulated micromechanical short crack driving force metrics. *Eng Fract Mech*. 2015;138:265-288.
13. Wang L, Daniewicz SR, Horstemeyer MF, Sintay S, Rollett AD. Three-dimensional finite element analysis using crystal plasticity for a parameter study of microstructurally small fatigue crack growth in a AA7075 aluminum alloy. *Int J Fatigue*. 2009;31(4):651-658.
14. Zhang X, Dunne FPE. 3D CP-XFEM modelling of short crack propagation interacting with twist/tilt nickel grain boundaries. *J Mech Phys Solids*. 2022;168:105028.
15. Hochhalter JD, Littlewood DJ, Veilleux MG, et al. A geometric approach to modeling microstructurally small fatigue crack formation: III. Development of a semi-empirical model for nucleation. *Model Simul Mater Sci Eng*. 2011;19(3):35008.
16. Castelluccio GM, McDowell DL. A mesoscale approach for growth of 3D microstructurally small fatigue cracks in polycrystals. *Int J Damage Mech*. 2014;23(6):791-818. Publisher: SAGE Publications Ltd STM.

17. Yaghoobi M, Stopka KS, Lakshmanan A, Sundararaghavan V, Allison JE, McDowell DL. PRISMS-fatigue computational framework for fatigue analysis in polycrystalline metals and alloys. *Npj Comput Mater*. 2021;7(1):38.
18. Hochhalter JD, Littlewood DJ, Christ RJ, et al. A geometric approach to modeling microstructurally small fatigue crack formation: II. Physically based modeling of microstructure-dependent slip localization and actuation of the crack nucleation mechanism in AA 7075-T651. *Model Simul Mater Sci Eng*. 2010;18(4):45004.
19. Fatemi A, Socie DF. A critical plane approach to multiaxial fatigue damage including out-of-phase loading. *Fatigue Fract Eng Mater Struct*. 1988;11(3):149-165. _eprint: doi:10.1111/j.1460-2695.1988.tb01169.x
20. Castelluccio GM, McDowell DL. Microstructure-sensitive small fatigue crack growth assessment: effect of strain ratio, multiaxial strain state, and geometric discontinuities. *Int J Fatigue*. 2016;82:521-529.
21. Musinski WD, McDowell DL. Simulating the effect of grain boundaries on microstructurally small fatigue crack growth from a focused ion beam notch through a three-dimensional array of grains. *Acta Mater*. 2016;112:20-39.
22. Srivastava S, Yaghoobi M, Sundararaghavan V. A graph-theoretic approach for multiscale modeling and prediction of crack propagation in polycrystalline materials. *Eng Fract Mech*. 2021;241:107406.
23. Li J, Proudhon H, Roos A, Chiaruttini V, Forest S. Crystal plasticity finite element simulation of crack growth in single crystals. *Comput Mater Sci*. 2014;94:191-197. IWCMM23 Special Issue.
24. Proudhon H, Li J, Wang F, Roos A, Chiaruttini V, Forest S. 3D simulation of short fatigue crack propagation by finite element crystal plasticity and remeshing. *Int J Fatigue*. 2016;82:238-246.
25. Pierson KD, Hochhalter JD, Spear AD. Data-driven correlation analysis between observed 3D fatigue-crack path and computed fields from high-fidelity, crystal-plasticity, finite-element simulations. *JOM*. 2018;70(7):1159-1167.
26. Pierson K, Rahman A, Spear AD. Predicting microstructure-sensitive fatigue-crack path in 3D using a machine learning framework. *JOM*. 2019;71(8):2680-2694.
27. Rovinelli A, Guilhem Y, Proudhon H, Lebensohn RA, Ludwig W, Sangid MD. Assessing reliability of fatigue indicator parameters for small crack growth via a probabilistic framework. *Model Simul Mater Sci Eng*. 2017;25(4):45010. Publisher: IOP Publishing.
28. Proudhon H, Li J, Ludwig W, Roos A, Forest S. Simulation of short fatigue crack propagation in a 3D experimental microstructure. *Adv Eng Mater*. 2017;19(8):1600721. _eprint: doi:10.1002/adem.201600721
29. Suter RM, Hennessy D, Xiao C, Lienert U. Forward modeling method for microstructure reconstruction using x-ray diffraction microscopy: single-crystal verification. *Rev Sci Instrum*. 2006;77(12):123905. Publisher: American Institute of Physics.
30. Greeley DA, Adams JF, Kenesei P, Spear AD, Allison JE. Quantitative analysis of three-dimensional fatigue crack path selection in Mg alloy WE43 using high energy X-ray diffraction microscopy. *Fatigue Fract Eng Mater Struct*. 2023. doi:10.1111/ffe.14217
31. Phung BR, Spear AD. A voxel-based remeshing framework for the simulation of arbitrary three-dimensional crack growth in heterogeneous materials. *Eng Fract Mech*. 2019;209:404-422.
32. Phung BR, He J, Spear AD. A surface-mesh gradation tool for generating gradated tetrahedral meshes of microstructures with defects. *Comput Mater Sci*. 2021;197:110622.
33. Spear AD, Hochhalter JD, Cerrone AR, et al. A method to generate conformal finite-element meshes from 3D measurements of microstructurally small fatigue-crack propagation. *Fatigue Fract Eng Mater Struct*. 2016;39(6):737-751.
34. Groeber MA, Jackson MA. DREAM.3D: a digital representation environment for the analysis of microstructure in 3D. *Integr Mater Manuf Innov*. 2014;3(1):5.
35. Si H. TetGen, a Delaunay-based quality tetrahedral mesh generator. *ACM Trans Math*. 2015;41(2):1-36. Publisher: ACM New York, NY, USA.
36. SIMULIA. Abaqus documentation 2022.
37. Savitzky A, Golay MJE. Smoothing and differentiation of data by simplified least squares procedures. *Anal Chem*. 1964;36(8):1627-1639. ISBN: 0003-2700 Publisher: American Chemical Society.
38. Kalidindi SR, Bronkhorst CA, Anand L. Crystallographic texture evolution in bulk deformation processing of FCC metals. *J Mech Phys Solids*. 1992;40(3):537-569.
39. Yaghoobi M, Ganesan S, Sundar S, et al. PRISMS-plasticity: an open-source crystal plasticity finite element software. *Comput Mater Sci*. 2019;169:109078.
40. Ganesan S, Yaghoobi M, Githens A, et al. The effects of heat treatment on the response of WE43 Mg alloy: crystal plasticity finite element simulation and SEM-DIC experiment. *Int J Plast*. 2021;137:102917.
41. Anand L, Kothari M. A computational procedure for rate-independent crystal plasticity. *J Mech Phys Solids*. 1996;44(4):525-558.
42. Githens A, Ganesan S, Chen Z, Allison J, Sundararaghavan V, Daly S. Characterizing microscale deformation mechanisms and macroscopic tensile properties of a high strength magnesium rare-earth alloy: a combined experimental and crystal plasticity approach. *Acta Mater*. 2020;186:77-94.
43. Castelluccio GM, McDowell DL. Microstructure and mesh sensitivities of mesoscale surrogate driving force measures for transgranular fatigue cracks in polycrystals. *Mater Sci Eng A*. 2015;639:626-639.
44. Erdogan F, Sih GC. On the crack extension in plates under plane loading and transverse shear. *ASME J Basic Eng*. 1963;85(4):519-525.
45. Arakere NK, Knudsen EC, Wells D, McGill P, Swanson GR. Determination of mixed-mode stress intensity factors, fracture toughness, and crack turning angle for anisotropic foam material. *Int J Solids Struct*. 2008;45(18):4936-4951.
46. Bayesteh H, Mohammadi S. XFEM fracture analysis of orthotropic functionally graded materials. *Compos B: Eng*. 2013;44(1):8-25.
47. Judt PO, Zarges J-C, Feldmann M, Ricoeur A, Heim H-P. Deflecting mode-I cracks in anisotropic materials. *Mech Mater*. 2019;136:103060.
48. Nejati M, Aminzadeh A, Amann F, Saar MO, Driesner T. Mode I fracture growth in anisotropic rocks: theory and experiment. *Int J Solids Struct*. 2020;195:74-90.
49. Bennett VP, McDowell DL. Polycrystal orientation distribution effects on microslip in high cycle fatigue. *Int J Fatigue*. 2003;25(1):27-39.

50. Schaef W, Marx M. A numerical description of short fatigue cracks interacting with grain boundaries. *Acta Mater*. 2012; 60(5):2425-2436.
51. Ludwig W, Buffière J-Y, Savelli S, Cloetens P. Study of the interaction of a short fatigue crack with grain boundaries in a cast Al alloy using X-ray microtomography. *Acta Mater*. 2003; 51(3):585-598.
52. Ohno N, Wang JD. Kinematic hardening rules with critical state of dynamic recovery, part I: formulation and basic features for ratchetting behavior. *Int J Plast*. 1993;9(3):375-390.
53. Zirkle T, McDowell DL. Analysis of monotonic and cyclic crack tip plasticity for a stationary crack tip in a FCC crystal. *Comput Mater Sci*. 2022;202:110954.
54. Quey R, Dawson PR, Barbe F. Large-scale 3D random polycrystals for the finite element method: generation, meshing and remeshing. *Comput Methods Appl Mech Eng*. 2011;200(17): 1729-1745.

How to cite this article: Phung BR, Greeley DA, Yaghoobi M, Adams JF, Allison JE, Spear AD. Predicting microstructurally sensitive fatigue-crack path in WE43 magnesium using high-fidelity numerical modeling and three-dimensional experimental characterization. *Fatigue Fract Eng Mater Struct*. 2023;1-22. doi:10.1111/ffe.14210

APPENDIX A: MESH CONVERGENCE

Global convergence was assessed on an uncracked microstructure, and local convergence was assessed on a microstructure with the initial crack inserted. The globally converged nominal element size, which was determined with a 5% error tolerance via the global stress-strain curve, was determined to be 42 μm. The locally converged element size, which is the local-element size where probe variables did not significantly change, was determined to be 4.2 μm. Furthermore, a separate test was conducted where the approximate global element size was varied from 9 μm to 36 μm, and the local kink angle predictions were not affected. The authors acknowledge that while these values cannot apply for all combinations of crack geometries and grain combinations, they do provide a valuable guideline for an absolute minimum. Furthermore, all simulations were run with mesh sizes that meet or exceed the requirement for mesh convergence.

APPENDIX B: CALIBRATION

In the current work, the critical resolved shear stresses (CRSS) of underaged WE43 Mg alloy were calibrated using the framework provided by Ganesan et al.[40] An initial microstructure was generated using the experimental electron back-scatter diffraction (EBSD) measurements as described in Ganesan et al[40] using Neper.[54] The CPFE simulations were conducted using PRISMS-Plasticity.[39] A $50 \times 50 \times 50$ FE cubic mesh was used to calibrate the sample. The elastic constants of underaged WE43 Mg used by Githens et al[42] and Ganesan et al[40] were incorporated for the WE43 Mg sample.

Ganesan et al[40] developed a calibration framework for WE43 Mg alloy at different heat treatment conditions in which the upper and lower bounds for CRSS of slip modes used to calibrate the CPFE simulation are defined using the contributions from lattice resistance, solute strengthening, and grain size effects. According to Ganesan et al,[40] the CRSS of underaged WE43 sample are bound to those of WE43-ST (lower bound) and WE43-T6 (upper bound). The calibrated CRSS values of WE43-ST and WE43-T6 (Ganesan et al.[40]) were used here as optimization upper and lower bounds for the underaged WE43 sample, which are presented in Table B1. The CRSS values for underaged WE43 Mg alloy were iteratively calibrated using the uniaxial tension response

TABLE B1 Optimization bounds provided for calibration of initial slip resistance for slip modes of underaged WE43 Mg alloy.[40]

Slip system	ST s_0^α (Lower bound) (MPa)	T6 s_0^α (Upper bound) (MPa)
Basal	22	47.6
Prismatic	72	92.2
Pyramidal<a>	74	104.5
Pyramidal<c+a>	77	117.3

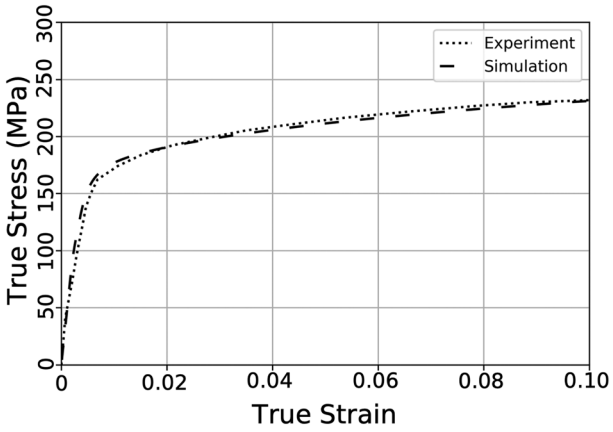

FIGURE B1 Stress-strain curve from calibrated crystal-plasticity parameters versus experimental data from Ganesan et al.[40]